Masterthesis

Atmospheric propagation of laser beams for the post-mission-disposal of satellites

Atmosphärische Propagation von Laserstrahlen zum Post-Mission Disposal von Satelliten

for obtaining the scientific degree
Master of Science

submitted by

Jakob Boventer

born 30/01/1993 in Cologne

German Aerospace Center e.V., Stuttgart
Institute of Technical Physics
Department Solid State Lasers and Nonlinear Optics

Stuttgart, 06/12/2019

Abstract

Human space flight is, historically speaking a new phenomenon, but there is already a multitude of man-made objects in orbit around the earth. The source of these objects is clear and so is the sink, which are the upper layers of the earths atmosphere. These layers slow objects down and accelerate their violent re-entry where most of them are burned up. Currently, the number of launched objects surpasses the number of removed ones. Therefore the orbit is getting crowded, which increases the risk of collisions. Removing small pieces of space debris is a challenging task, but removing cooperative satellites which have been designed from the beginning considering a controlled de-orbit is a slightly easier task. One way of achieving this is a laser ablative propulsion unit which delivers the thrust needed for the post-mission disposal, powered by a ground based laser station. This laser has to propagate through the atmosphere to reach the satellite and the properties of the arriving beam after getting influenced by the atmosphere have to be known. Hence the interaction of the laser beam with the atmosphere has to be modelled in the context of a post-mission disposal of a satellite.
The focus in this thesis is on modelling this atmospheric propagation of laser beams, with special attention paid to atmospheric turbulence. In the beginning the most important theoretical knowledge about the earths atmosphere, the phenomenon of turbulence in general and about statistics are explained. Following this is an overview about the way the distribution of turbulence in the atmosphere is modelled, and three models are picked and explained, supplemented by one measurement. Afterwards the available models for this thesis are presented, one is a numerical one implemented in a program called AtmProp. The other one is based on analytical formulae. These models have been supplemented by a model for the height distribution of turbulence via a program written on python basis, developed in the course of this thesis. Once all the programs and models were available, two tests have been conducted, one verifying the numerical model for an undisturbed beam and the other one comparing different turbulence distribution models to each other. Following this different examples were calculated with the focus on a comparison of the numerical model and the analytical model. In addition the influence of different initial beam properties such as beam diameter, radius of curvature and initial beam shape with different turbulence conditions have been investigated. It became clear during this thesis that for the final beam arriving at the target the level of turbulence is more important than the initial beam parameters. The turbulence is removing the differences of the initial beams, making them independent of their initial parameters arriving at the target. At the end one example of a post mission disposal with a implemented turbulence model was calculated, to see if the concept of a post-mission disposal with a laser ablative propulsion is feasible considering atmospheric turbulence. Without turbulence compensation, feasibility is unclear, but with a well-working adaptive compensation technique it should become feasible. To develop and test ways of turbulence compensation in future work, modelling the propagation of laser beams in a turbulent atmosphere is a necessity.

Zusammenfassung

Die menschliche Raumfahrt ist ein vergleichsweise neues Phänomen, trotzdem befindet sich aktuell bereits eine hohe Anzahl von menschengemachten Objekten im Orbit. Die Quelle dieser Objekte ist offensichtlich, die Senke liegt auch nahe. Die oberen Schichten der Atmosphäre repräsentieren die Senke, da sie Objekte, die in ihrem Einflussbereich sind weiter abbremsen. Damit verlieren die Objekte zusätzlich an Höhe und sind einer steigenden Luftdichte mit abnehmender Höhe ausgesetzt. In Kombination mit hohen Eintrittsgeschwindigkeiten führt dies zu hohen Wärmelasten die zum verglühen dieser Objekte führt. Aktuell ist die Anzahl an Objekten die hinzukommen deutlich höher, als die Anzahl von Objekten die verglühen. Dies erhöht die Gefahr von Kollisionen. Die Entfernung von kleinen Objekten ist eine komplexe Aufgabe, die Entfernung von kooperativen Satelliten deutlich einfacher. Eine Option um den benötigten Schub für einen De-Orbit auf den Satelliten aufzubringen, ist die Verwendung von einem Laser-ablativen Antriebsmodul. Der vom Boden ausgehende Laser propagiert durch die gesamte Atmosphäre. Auf dem Weg ist der Strahl dem Einfluss der Atmosphäre ausgesetzt. Um eine sinnvolle Auslegung auf der Satellitenseite zu ermöglichen, ist die Kenntnis der Eigenschaften des Strahls am Ziel notwendig. Daher muss die Interaktion des Lasers mit der Atmosphäre im Kontext eines kontrollierten De-Orbits modelliert werden. Der Fokus dieser Arbeit liegt auf der Modellierung der Ausbreitung des Laserstrahls, mit Schwerpunkt auf atmosphärischer Turbulenz. Als erstes werden die grundlegenden Phänomene dargelegt. Den Anfang macht eine Zusammenfassung der wichtigsten Erkenntnisse, die über den Aufbau der Atmosphäre vorliegen, gefolgt von einer allgemeinen Einführung in die Thematik der Turbulenz. Daran schließt sich eine kurze Erläuterung der Statistik an. Die Methodik zur Modellierung von der Höhenabhängigkeit atmosphärischer Turbulenz wird präsentiert und drei Modelle werde ausgesucht. Ergänzend wird auch eine verfügbare Messung verwendet. Zwei Modelle zur Modellierung der Turbulenzeffekte werden verwendet, ein numerisches, was in dem Programm AtmProp implementiert ist, und ein analytisches. Diese Modelle werden durch ein im Laufe der Arbeit entwickeltes Python Programm ergänzt, um die Höhenverteilung der Turbulenz abzubilden. Nachdem alle Modelle und Programme verfügbar waren wurden zwei Tests durchgeführt, der erste um das numerische Modell für einen ungestörten Strahl zu verifizieren, und der zweite um die unterschiedlichen Modelle für die Höhenverteilung der Turbulenz zu vergleichen. Im Anschluss wurden verschiedene Beispiele berechnet um das analytische und das numerische Modell miteinander zu vergleichen. Im Zuge dieser Berechnungen wurde der Einfluss von unterschiedlichen Parametern des gesendeten Strahls wie Strahldurchmesser, Krümmungsradius und das anfängliche Profil des Strahls in Kombination mit unterschiedlichen Turbulenzbedingungen untersucht. Im Laufe der Arbeit wurde klar, das die Stärke der Turbulenz für den ankommenden Strahl wichtiger ist als die Startparameter. Turbulenz entfernt den Unterschied der Strahlen, was den ankommenden Strahl von den anfänglichen Parametern unabhängig macht. Am Ende der Arbeit wird ein beispielhafter Fall eines De-Orbits berechnet, um zu untersuchen ob sich eine Mission wie diese mit atmosphärischer Turbulenz lohnt. Kombiniert mit einer leistungsfähigen Technik zur Turbulenzkompensation ist es definitiv lohnenswert ohne ist dies fraglich. Um Methoden zur Turbulenzkompensation entwickeln und testen zu können, ist die Modellierung der Propagation von Laserstrahlen in turbulenter Atmosphäre eine Notwendigkeit.

Contents

Nomenclature

Latin Letters

Symbol	Description	Unit
n	Refractive index	-
T	Temperature	K
T_r	Reference temperature at reference height	K
T_0	Temperature at zero level	K
P_0	Pressure at zero level	mb
Re	Reynolds number	-
L	Characteristic length	m
v	Speed of the flow	$\frac{m}{s}$
$\boldsymbol{r}$	Radius vector	m
B	Covariance function	-
$\boldsymbol{K}$	Vector wave number	$\frac{1}{m}$
D_v	Structure function of the velocity	$\frac{m^2}{s^2}$
D_n	Structure function of the refractive index	-
C_v^2	structure velocity constant	$m^{\frac{4}{3}} s^{-\frac{8}{3}}$
C_n^2	refractive index structure constant	$m^{-\frac{2}{3}}$
$C_n^2(h)$	structure velocity constant as a function of height	$m^{-\frac{2}{3}}$
$C_n^2(h_r)$	structure velocity constant for reference height	$m^{-\frac{2}{3}}$
${}^{eq}C_n^2(h_u)$	Structure function on a height-equally spaced grid	$m^{-\frac{2}{3}}$
${}_u^{eq}C_n^2(h_u)$	Values of the structure function on a h equally spaced grid for step u	$m^{-\frac{2}{3}}$
${}_jC_n^2(h_j)$	Values of the structure function on a C_n^2 equally spaced grid for step j	$m^{-\frac{2}{3}}$
${}_q^I C_n^2(h_q^I)$	Values of the structure function for the $h^{eq}_{u_{min-1}}$ to $h^{eq}_{u_{min+1}}$ Interval	$m^{-\frac{2}{3}}$
l_0	Inner scale of turbulence	m
L_0	Outer scale of turbulence	m
k	wave vector	$\frac{1}{m}$
k_{karman}	Von Karman constant	-
E	Electric field	$\frac{V}{m}$
t	Time	s
t_h	Temporal hour	-
z	Cartesian coordinate	m
x	Cartesian coordinate	m
y	Cartesian coordinate	m

c	Speed of light in vacuum	$\frac{m}{s}$
H	Final propagation distance	m
h	Height above ground level	m
h_z	Roughness height	m
h_s	Height above sea level	m
h_0	Height above ground used for $C_n^2(h_0)$	m
h_r	Reference height for ARL model	m
h_{ini}	Height of first inversion layer for ARL model	m
h_u^{eq}	Height of step u in the equally spaced height grid	m
$h_j({}_jC_n^2)$	Height values on the equally spaced C_n^2 grid	m
$h(C_n^2)$	Height as a function of the structure constant	m
h_{apo}	Apogee height of the satellite	m
h_{peri}	Perigee height of the satellite	m
W	Root mean square of wind speed in the atmosphere	$\frac{m}{s}$
u_r	Average wind speed for ARL model at reference height	$\frac{m}{s}$
r_0	Coherence diameter	m
M	Parameter of the HAP turbulence model	-
M_{laser}	Beam product of a laser	-
p	Coefficient for the HAP model	-
g	Gravitational acceleration	$\frac{m}{s^2}$
A	Dry-Air wavelenght dependence function for $\lambda = 500nm$	$\frac{K}{mb}$
j	Index of segments for the different propagation steps	-
z_j	position of the segment j	m
Δz_j	Propagation distance from z_j to z_{j+1}	m
$z_{propdir}$	Propagation distance from telescopes exit	m
w_{Init}	2nd moment beam radius az the telescopes exit	m
f	Focal distance of the sending telescope	m
f_{Rep}	Laser repetition rate	Hz
$w(z)$	2nd moment beam radius at position z	m
w_{LT}	2nd order moment of beam radius long-term	m
w_{ST}	2nd order moment of beam radius short-term	m
$w_{numeric}$	2nd order moment beam radius of numeric solution at final propagation distance	m
$w_{analytic}$	2nd order moment beam radius of analytic solution at final propagation distance	m
n_C	Number of cases to calculate	-
${}^Rz_0$	Rayleigh range of the gaussian beam	m
R	Radius of curvature of the propagating wave	m
w_0	2nd order moment beam radius at the beam waist (wave-optical focus)	m
z_{wave}	Cartesian z-coordinate from the beam waist(wave-optical focus)	m
P	Power of the Laser	W
I	Intensity	$\frac{W}{m^2}$
r_x	2nd moment of the numeric beam in x direction	m
r_y	2nd moment of the numeric beam in y direction	m

r_{circ}	2nd moment of the numeric beam with circular shape and equal surface area	m
m_{sat}	Mass of the satellite	kg
In	Inklination of the satellites orbit	
Δv	Velocity difference of the satellite	$\frac{m}{s}$
D_{spot}	Beam spot diameter on the ablative target	cm
D_{rec}	Diameter of the receiver on the satellite	m
E_P^{GS}	Pulse energy of the laser	J

Greek letters

Symbol	Description	Unit
ε	Turbulent energy dissipation rate	W
ν	Kinematic viscosity	$\frac{s}{m^2}$
ρ	Density	$\frac{kg}{m^3}$
$\xi(\boldsymbol{r})$	A three dimensional field	-
ξ_H	Dimensionless height normed to final propagation height	-
ϕ_ξ	Power spectrum of ξ	-
λ	Wave-lenght of an electromagnetic wave	m
∇	Nabla operator	$\frac{1}{m}$
ϵ	Permitivity	$\frac{F}{m}$
Γ	phase shift of electromagnetic wave	-
σ_{jitter}	Standard deviation of the telescopes alignment	$\mu grad$
β_w	Beam wander contribution to 2nd order moment beam radius	m
ζ	Zenith angle of a target in orbit	rad

Abbreviations

HV	Hufnagel-Valley
HAP	Hufnagel-Andrew-Philips
ARL	Atmospheric research Llb
ROC	Radius of curvature
LIC	Laser irradiation contact

List of Figures

List of Tables

1 Introduction

Since humans started exploring and utilizing space in 1957, [10] the number of objects as well as the mass of man made objects in orbits around earth is increasing.
In addition as the probability of collisions which are releasing numerous new objects is rising the probability of further collisions, something refereed to as the Kessler effect first mentioned by Kessler in 1978 [14].
The natural sink of objects is the interaction with the upper layers of the earth's atmosphere with the effect that their orbit is further decreasing, through slowed down by aerodynamic forces. This forces, in addition with high heat fluxes, leads to the destruction of many objects before they arrive at earth's surface. Not all objects are completely destroyed, especially large structures tend to crash into the ground at some point. This requires avoiding damage on the ground. Nevertheless, one source of new space debris in the future will be objects which are already in space by now. Additional objects will be launched, which will contribute to the amount of space debris orbiting the earth.
This has to be kept in mind designing new satellite and new missions, because they have to offer a possibility to be removed from space either by de-orbit or by moving them to a grave-yard orbit after reaching the end of their service life.
In order to de-orbit an object a delta-v is needed, which requires additional mass and additional systems on the satellite which can deliver this delta-v, increasing the weight and the complexity of the spacecraft, driving up launching and development costs.
Alternatively to carrying the required energy with some kind of fuel, a ground based laser to transport energy and to manipulate objects in orbit. One issue arising here is that the the laser beam has to travel the distance between the ground station and the target in the atmosphere, crossing through different atmospheric layers with different densities, temperatures and other properties. These properties and other factors are influencing the propagating laser beam, and the influence on the beam has to be estimated in order to enable a user to design missions and satellites which benefit from the laser beam. Hence, information about the beam are needed at is position where a potential system wants to use it, after propagating the whole distance from the ground station to the object in question. The most important influence is the one of the refractive index fluctuations which are in the focus of this thesis.
To get an idea about the different existing models, which are investigated in this thesis, in addition to the investigation of different turbulence models. This is necessary because alone getting a model for the refractive index turbulence is a complex task where many authors already have contributed to.
This thesis is using a numerical model implemented in a software tool named AtmProp, as well as a analytical model and different turbulent models for the turbulence in different heights.
In chapter 2 the theoretical backgrounds are explained, followed by a presentation of two different ways for modelling the propagation in chapter 3. Chapter 4 is showing which simulations have been conducted for this thesis and show the most important results of these. In addition the two different models are compared to each other for these simulations. In the end chapter 5 shows one exemplar De-orbit calculation.

2 Theoretical background

A wave-optical propagation through the whole atmosphere is requiring knowledge from different fields since multiple different topics are having an effect on the wave which arrives at the target after the propagation. The important fields for evaluating a post-mission disposal of a satellite with a ground based laser are summarized in the following sections of this chapter. The earths atmosphere is summarized in section 2.1, Turbulence in section 2.2, the mathematical concepts of statistics including kolmogorovs theory in section 2.3, and the interaction of the propagating wave with the medium it is crossing in section 2.4. The knowledge presented here is essential to understand the implications influencing the design of a post-mission disposal mission. Additionally the theory presented here is the basis to model the wave-optical propagation with different approaches, this modelling is investigated in further detail in chapter 3.

2.1 The earth's atmosphere

Figure 2.1: Atmospheric layers visible from the international space station. The lower part is the earths limb followed by the orange troposphere, containing dark clouds. Above it is the stratosphere, in pink and the upper atmosphere in blue followed by open space which appears black [19].

Between the outer solar atmosphere and the ground is the earth's atmosphere, a mainly gaseous part of the earth which is surrounding the solid part of the planet, stretching from the surface to a distance of approximately 600 km where the Exosphere begins, which also represents the transition to interplanetary space [1]. Figure 2.1 shows a photography of a sunset from the International space station.This indicates a fact which is used in order to model the atmosphere: it can be divided into different layers which exhibit particular properties.
In order to influence any objects in orbit around earth by using a laser beam from a ground station the laser beam has to travel from the station to the targets.
These targets can be satellites in low-earth orbits, or non-cooperative pieces of space debris which are constituting a threat to satellites.
Electromagnetic waves, like laser beams propagating through this medium experience different effects, the three most important being: absorption, scattering and refractive-index fluctuations (optical turbulence) [1].
To get a complete picture of laser beam propagation and especially to design potential systems all relevant effects have to be modelled. Since modelling absorption and scattering would exceed the scope of this thesis, the focus in this thesis is on optical turbulence and its effects on the propagation of laser beams.
Optical turbulence mainly depends on gradients of the refractive index n which is an intensive property of a fluid just as temperature T, density ρ, and concentration of a substance. Intensive here means that changing the amount of considered fluid is not changing its value. The properties of a fluid depend a lot on is composition of it. Determining the exact composition is complicated due to the fact that it changes with the position in the atmosphere, the time of the year, and at least close to the ground, also on the time of the day. The most important gaseous compounds of the atmosphere are nitrogen, oxygen, water vapour, carbon dioxide, nitrous oxide, carbon monoxide and ozone [1]. Beside the gaseous and liquid elements there are also solid elements like dust particles of different sizes in the earths atmosphere.
To help regularising this complexity a standard atmosphere can be defined.
One common example is the international standard atmosphere according to the ISO 2533:1975 norm. This standard is splitting up the atmosphere into different sections, the troposphere, stratosphere, mesosphere and the thermosphere, based on the vertical temperature gradient. Figure 2.2 shows the different temperature gradients as well as the different sections of the atmosphere according to this standard.

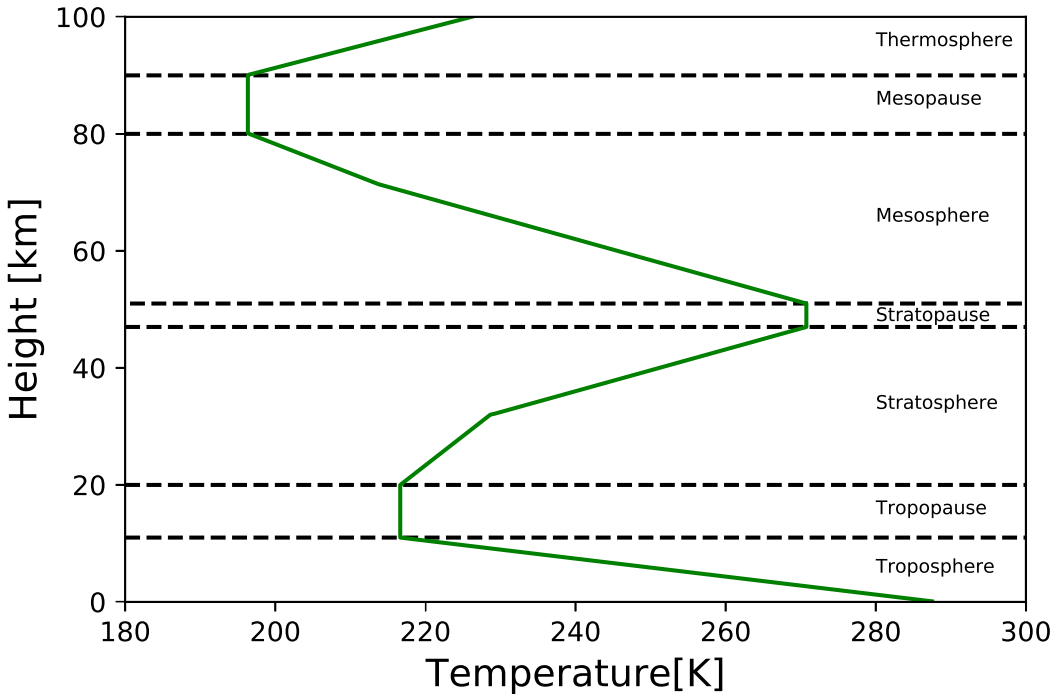

Figure 2.2: Temperature distribution and gradients in the earths atmosphere, supplemented by the names of the atmospheric layers according to ISO2533.

The dynamics of the atmospheric system are mainly governed by orbital dynamics of the earth relative to the sun and therefore depends on the geographical location, the time of the day, as well as the time of the year. Note that there exists an atmospheric boundary layer, which defines the distance from the ground up to which the daily fluctuations are showing an impact.
The suns radiation has different effects on the earth and on earths atmosphere mainly causing gradients of temperature, density, speed of moving air, and pressure resulting in winds and complex systems of mass and energy transport in the atmosphere represented by small scale and big scale weather phenomena. It is these transport mechanisms which are the main cause of optical turbulence, a phenomena explained in the following section in further detail in the scope of laser beam propagation in random media.
For the case of Post-Mission disposal the structure of the atmosphere has some implications, the most important one is the fact that the troposphere is the most dense part containing roughly 75 % of the atmospheric mass.
Additionally most of the weather and the convective activity due to the suns radiation occurs here [1].
Due to the fact that the distortion of a Laser Beam due to atmospheric effects depends on the density of the air, it is a valid assumption that the beam is experiencing the biggest distortion in the troposphere and the lower stratosphere.
As a consequence the utilized turbulence models in this thesis are applied till a height above ground of 30 km and from there a distortion free propagation is assumed.

2.2 Turbulence

Considering a flowing viscous fluid two basic "states" of the flow are distinguished one called laminar and the other one turbulent.
The first one is characterized by a regular motion, parallel streamlines and no velocity fluctuations relative to the main flow.
The second one on the other hand is a more chaotic state, with random fluctuations far from equilibrium and complex deviations from the main flow. In addition turbulent flows are non-stationary, dissipative and exhibit increased levels of diffusive transport. In the context of propagating laser beams this becomes important since wind and density fluctuations directly affect the refractive index of air.
The parameter commonly used to decide if a flow is turbulent or laminar is called the Reynolds number as written in equation 2.1, with L being a characteristic length in meters, v being the velocity in $\frac{m}{s}$ and ν being the kinematic viscosity in $\frac{s}{m^2}$.

$$Re = \frac{L \cdot v}{\nu} = \frac{Inertial forces}{Viscous forces} \tag{2.1}$$

It can be shown that the Reynolds number is basically describing which forces are dominating the dynamics of the flow, inertial ones on the one hand or viscous ones on the other hand.
In case of high Reynolds numbers the viscous forces, which tend to damp disturbances through dissipating energy into heat, can not outweigh the inertial forces. Disturbances can grow from small velocity fluctuations to big, complex systems of instabilities like eddies and vortices.
Therefore to transit from the laminar to the turbulent state a flow needs to experience a velocity gradient and exhibit a high Reynolds equation.
The order of magnitude considered a "high" Reynolds number depends on the specific flow taken into account,for instance the Reynolds number for the axial-symmetric jet shown in figure 2.3 is $Re = 10000$ [16].

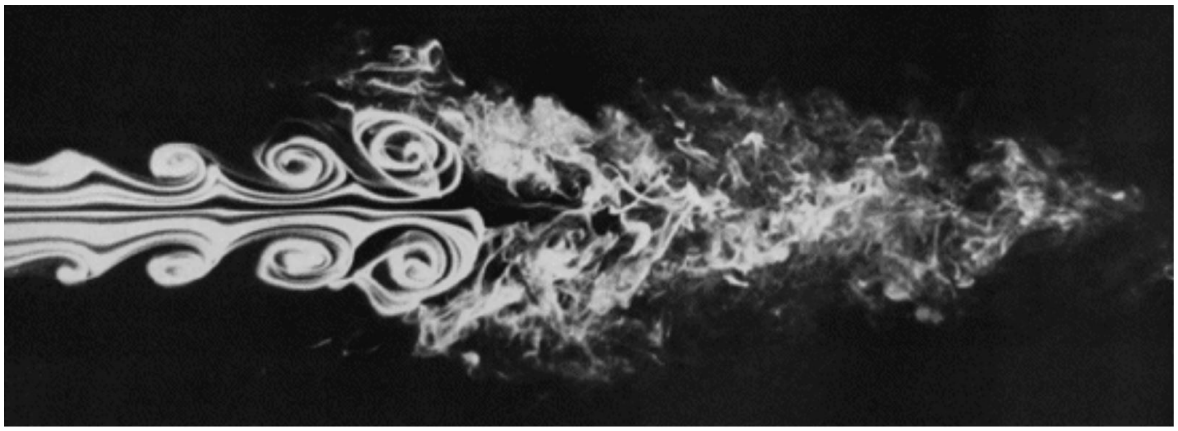

Figure 2.3: Instability of a axial-symetric jet Re=10000 [16].

The presence of the kinematic viscosity in the Reynolds number highlights the connection of the properties of the considered fluid and the occurrence of turbulence.
An approach to tackle turbulence directly would demand solving the Navier-Stokes equations. Since these (non-linear) equations are not closed per-se, a method to close them has to be chosen and implemented. Two examples for models like these are the eddy viscosity approach and the Reynolds-tension-transport models [16].
It has to be noted that all turbulence models are only mimicking the real processes to a

certain precision level [16].
Alternatively, a statistical description can be used, where especially the one developed by Kolmogorov [15] is worth to be mentioned. He derived it from dimensional analysis, following a description from Richardson [21], which is detailing the energy transport in a turbulent flow, by distinguishing eddies regarding their size relative to two fixed lengths: the inner scale called l_0 and the outer scale called L_0.Kinetic energy extracted from the main flow creates eddies of characteristics size L, dominated by inertial forces. These eddies decompose into smaller eddies till exhibiting the inner scale l_0 at which viscous effects become strong enough to dissipate them into heat.This size range is called the inertial range and inside this range fluctuations are assumed to be spatially homogeneous and isotropic [22].
It has to be noted here that the common literature dealing with turbulence is focusing on velocity fluctuations, but for the propagation of laser beams the refractive index is more important and hence the focus is laid on this attribute.
Figure 2.4 is showing the energy cascade, including the inertial subrange where energy is transported from big eddies to smaller eddies. The y-axis shows this so-called logarithm of the energy and the x-axis the scale of the eddies. The production of turbulent energy is on the left side of the energy cascade and the dissipation is on the right side. Turbulent energy is the energy taken from the main flow and later dissipated into heat.

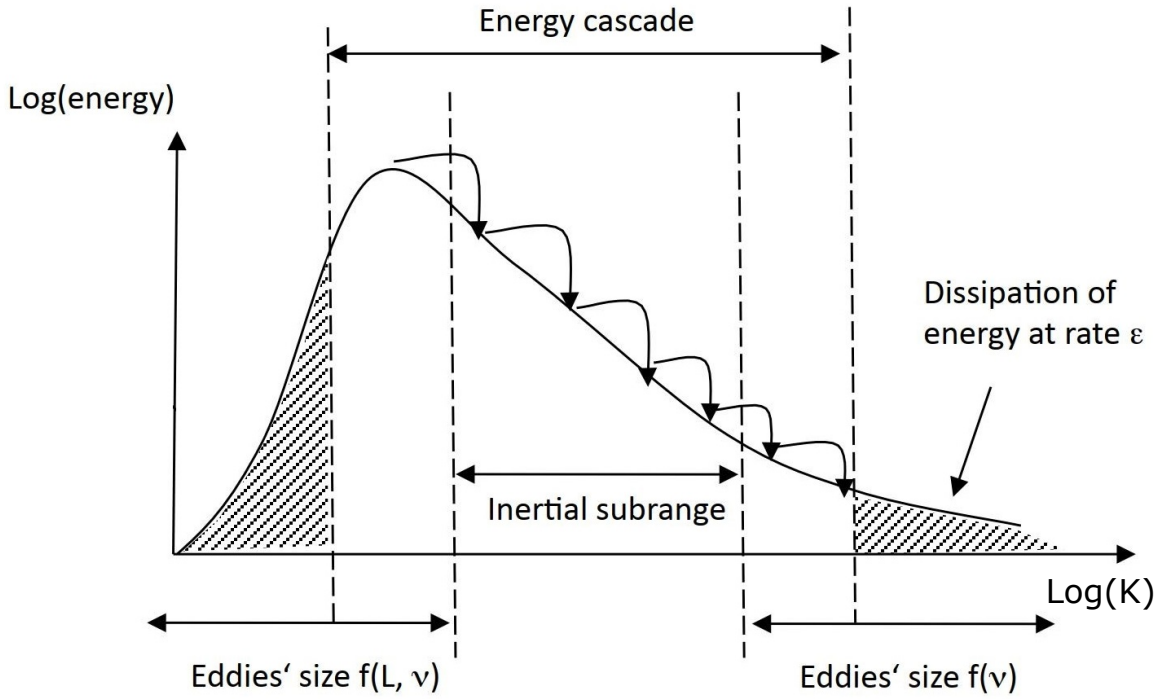

Figure 2.4: Energy cascade in turbulence, illustrated with the production rate and the disspation rate [16].

2.3 Statistics

As explained beforehand turbulence is a random process and it is not possible to model it deterministically. To analyse random processes the main two quantities defined, are the variance and the covariance [22]. The variance measures the degree of variation between a

measured value and the mean value, while the covariance is measuring the degree of variation between two measured values.
Generalising to a three dimensional field and assuming $\xi(\boldsymbol{r})$ being a three dimensional random field, the spatial covariance for two points r_1, r_2 of a homogeneous process is defined as:

$$B_\xi(\boldsymbol{r_1},\boldsymbol{r_2}) = \langle \xi(\boldsymbol{r_1})\xi(\boldsymbol{r_1}+\boldsymbol{r_2})\rangle - \langle\xi\rangle^2 \tag{2.2}$$

The power spectrum $\phi_\xi(\boldsymbol{K})$ is the three-dimensional Fourier transform of the covariance, with $\boldsymbol{K}$ being the vector wave number. This is also used to describe the distribution of energy in turbulent problems.

$$\phi_\xi(\boldsymbol{K}) = \left(\frac{1}{2\pi}\right)^3 \int\int\int_{-\infty}^{\infty} B_\xi(\boldsymbol{r}) e^{i\boldsymbol{K}\cdot\boldsymbol{r}} d\boldsymbol{r} \tag{2.3}$$

The inverse relation is :

$$B_\xi(\boldsymbol{r}) = \int\int\int_{-\infty}^{\infty} \phi_\xi(\boldsymbol{K}) \cdot e^{-i\boldsymbol{K}\cdot\boldsymbol{r}} d\boldsymbol{K} \tag{2.4}$$

Equation (2.4) is diverging for the turbulence spectrum from equation (2.11), in contrast to the structure function of ξ defined according to equation (2.5), which is not diverging.

$$D_\xi(\boldsymbol{r_1},\boldsymbol{r_2}) = \langle [\xi(\boldsymbol{r_1}) - \xi(\boldsymbol{r_2})]^2 \rangle \tag{2.5}$$

$$D_\xi(\boldsymbol{r}) = 2\int\int\int_{-\infty}^{\infty} \phi_\xi(\boldsymbol{K})\,[1 - cos(\boldsymbol{K}\cdot\boldsymbol{r})]\,d\boldsymbol{r} \tag{2.6}$$

it can be shown that the spectrum of the covariance is the same as the spectrum corrsponding to the structure function [22]. The structure function can also be applied in non-homogenous problems in which the covariance is not well-defined.

2.3.1 Kolmogorov's theory

Kolmogorov showed in his work that in the inertial range the longitudinal structure function of wind velocity satisfies a $\frac{2}{3}$ power law, with C_v^2 being the velocity structure constant as written in equation 2.8 [22].

$$D_v(r) = C_v^2 r^{\frac{2}{3}},\ l_0 < r < L_0 \tag{2.7}$$

$$C_v^2 = 2\varepsilon^{\frac{2}{3}} \tag{2.8}$$

For velocity fluctuations the inner scale is calculated with 2.9, taking into account the energy dissipation rate ε and the kinematic viscosity ν.

$$l_0 = \left(\frac{\nu^3}{\varepsilon}\right)^{(\frac{1}{4})} \tag{2.9}$$

Similar to the structure function for velocity $D_{rr}(r)$ a structure function $D_n(r)$ for refractive index fluctuations can be defined:

$$D_n(r) = C_n^2 r^{\frac{2}{3}},\ l_0 < r < L_0 \tag{2.10}$$

It can be shown that the corresponding the three dimensional power spectrum reads [24]:

$$\phi_n(K) = 0.033 C_n^2 K^{\frac{-11}{3}}. \tag{2.11}$$

The spectrum is giving information about the distribution of energy over the different spacial wavelengths of the fluctuations. Equation (2.11) shows the Kolmogorov spectrum which is not converging, regarding the inner scale l_0 and the outer scale L_0.
An alternative spectrum which converges for big outer scales L_0 and for small inner scales l_0, is the Karman spectrum shown in equation (2.12). This difference is also shown in figure 2.5, the orange line shows the Karman spectrum and the blue one the Kolmogorov spectrum, for $l_0 = 1\,cm$ and $L_0 = 100\,m$.

$$\phi_n(K) = \frac{0.033C_n^2}{\left(K^2 + \left(\frac{2\pi}{L_0}\right)^2\right)^{\frac{11}{6}}} \cdot e^{\frac{K^2}{\frac{5.91}{l_0}}} \tag{2.12}$$

The inner scale represents the scale of the turbulence where dissipation is taking place and therefore converting turbulent kinetic energy to heat.
The outer scale is the scale where energy is extracted from the main flow and converted to turbulent energy. Scale always refers to the wave-number associated with the according fluctuations. This theory was supplemented by Tatarski [24] who developed the basics to describe the interaction of turbulence and light propagating in a turbulent medium.

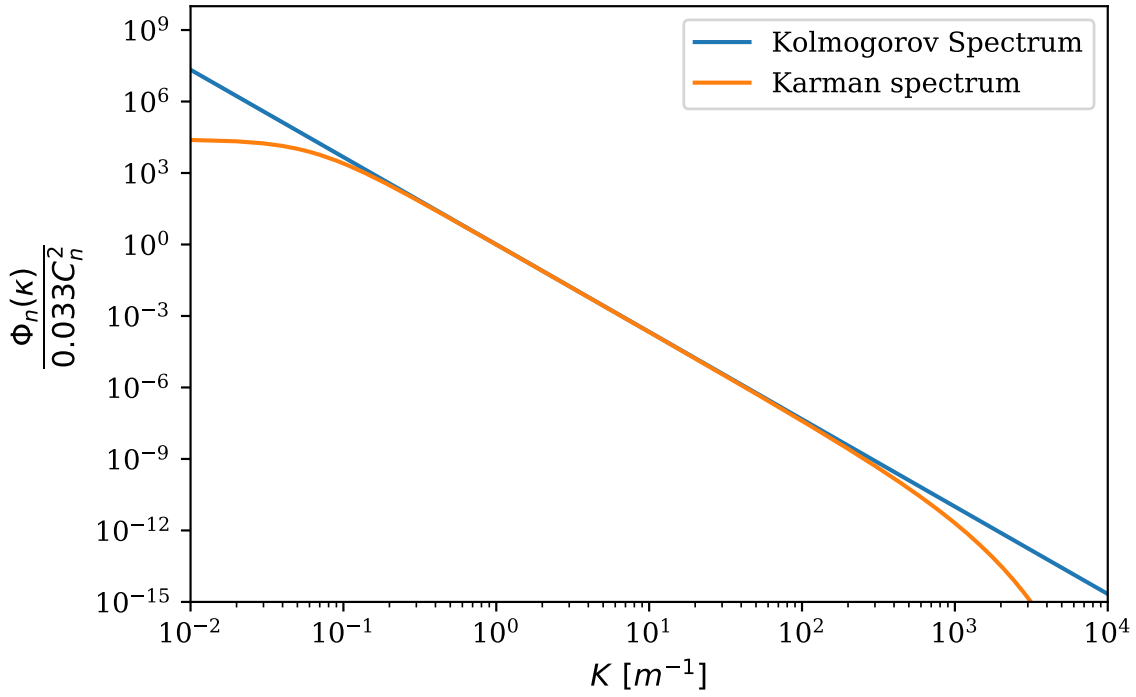

Figure 2.5: Kolmogorov and karman spectrum plotted logarithmic on both axes.

2.4 Light-air interaction

Light in general is an electromagnetic wave which is similar to to radio waves but exhibiting a higher frequency ν and a shorter wavelength λ. The electromagnetic field can be characterized by the electric field E, the magnetic field H and the wave vector. In the case of homogeneous, isotropic and unconfined media all three vectors are perpendicular to one another and the

wave vector k points into the direction of the propagation of the wave.
Since the electric field and the magnetic field are coupled, it is common to consider only the electric field [12].
Maxwells equations for a monochromatic (narrow frequency bandwidth) wave are used to describe the propagation of light through turbulence. Since there are multiple different forms of this equations the equations used by Fleck, which are also used in this thesis are presented here. The theoretical work behind the software is mainly derived from Fleck [13] and was implemented in the program AtmProp.
According to Fleck the Maxwell wave equation in the Fresnel approximation is:

$$2ik\left(\frac{n}{c}\frac{\partial E}{\partial t}+\frac{\partial E}{\partial z}\right)=\nabla_{\perp}^{2}E+k^{2}(n^{2}-1)E \tag{2.13}$$

Rewriting equation 2.13 for retarded time $t'=t-\frac{nz}{c}$ yields[13]:

$$2ik\frac{\partial E}{\partial z}=\nabla_{\perp}^{2}E+k^{2}\delta\epsilon E \tag{2.14}$$

The refractive index in equation (2.14) has been replaced with the permittivity ϵ which is linked to n via equation (2.15). The δ is denoting that the difference of ϵ or n is used here and not the absolut values of these variables.

$$\delta\epsilon=n^{2}-1\approx 2\delta n \tag{2.15}$$

Density gradients over the propagation path are causing changes in the speed the waves are travelling at, and since this gradients are not homogeneously distributed in the earths atmosphere waves are experiencing different magnitudes of it depending on their location in a moving wave front. In the course of this thesis the wave front is a laser beam with a spatial extension in x and y direction, perpendicular to the propagation vector k.
Quantifying this change of the speed in terms of a phase shift of the travelling waves, Fleck [13] is describing this phase shift as written in equation 2.16.
This equation describes the phase shift as a function of the δn over a distance Δz:

$$\Gamma(x,y)=\int_{z_n}^{z_n+\Delta z}\delta n(x,y,z)dz \tag{2.16}$$

The correlation between index of refraction formulations δn and the Kolmogorov spectrum is:

$$\langle\delta n(\boldsymbol{r_1})\delta n(\boldsymbol{r_2})\rangle=\int d^{3}\boldsymbol{K}e^{i\boldsymbol{K}\cdot(\boldsymbol{r_1}-\boldsymbol{r_2})}\phi_n(\boldsymbol{K}) \tag{2.17}$$

Inserting equation (2.17) into equation(2.16), the phase shift of a light wave can be calculated. Since this is a part of the AtmProp model, the implementation of these formulae is shown in section 3.1. In addition to the effects of turbulence, in his work Fleck is also considering the effects of thermal blooming, which is the change of the density of the air caused by the heating of it through absorption by the laser beam. This effect will be neglected in the course of this thesis.
Hence in the following sections and chapters the term phase shift is always refering to the phase shift caused by density gradients which exist in the turbulent atmosphere without depending on the laser beam.
Fleck uses the "phase screen" method which is also used for this thesis due to the fact that it is implemented in the utilized software AtmProp.

2.5 Turbulence models of the atmosphere

Figure 2.6: Images of thermal plumes rising from a heated surface in a fluid. As they rise they break-up due to viscous forces. [2][23]

A laser beam propagating through the atmosphere on its way to a target in orbit is crossing the complex and dynamic system of the earths atmosphere.
Depending on height above a reference value the atmosphere can be grouped into different layers which surround the earth like the layers of an onion. Therefore, the assumption of a constant value for the the turbulence structure constant C_n^2 is rendered wrong and demands a dependence on height: $C_n^2(h)$. As a result of the complexity of this task multiple models, with multiple different scopes and for multiple locations have been developed. Hence, the number of models used in this thesis had to be limited and three models have been chosen and implemented in Python.
The Hufnagel-valley model(HV) is the most common one which is due to the fact that it is simple to implement, depends only on two free parameters and is independent from the location on earth. Its biggest disadvantage is the way the lowest layer of the ground is modelled which does not correspond well to experimental evidence [2].
Therefore the HAP-model has been developed as an extension to the HV-model. Additionally to the HV and HAP models the Army Research Lab model (ARL) has been taken into account as an example of a rather complex parametric model. It combines different models to enable military planners to estimate the effects of turbulence in war scenarios [8].
To supplement these parametric models measurements have been used to show that, although its values are specific for a particular location (Mt. Graham) they are still close to the models regarding the order of magnitude [17].
Figure 2.6 shows an example of a heated surface and rising pockets of fluid which break up due to viscous forces. Although the fundamental physical parameters (density and viscosity) are orders of magnitude larger than in air the physical process is similar. It therefore serves to visualize the rise of air plumes from earths surface after being heated due to the increase of the ground temperature from the sun.

2.5.1 Mt. Graham measurements

In the following the three parametric models taken into account in this thesis are presented with one plot of an exemplar calculation for each single model. To show that the values calculated by these models are in a realistic range a paper from Masciadri et al.[17] was used. In this paper measurements at the Mt. Graham International Observatory (MGIO), located in the United states in the federal state of Arizona. The measurements are taken at fourty-three different nights with a generalized SCIDAR (GS) [17].
This technique is a modification of the classic SCIDAR technique and "relies on the analysis of the scintillation images generated by a binary in the pupil plane of a telescope" [18].
The ARL, HV and HAP model have been calculated and the median values from E. Masciadris measurements have been inserted, after converting them by shifting the zero because Masciadris values are starting on a mountain top, in contrast to the other models which are starting at ground level.

2.5.2 Hufnagel-Valley model (HV)

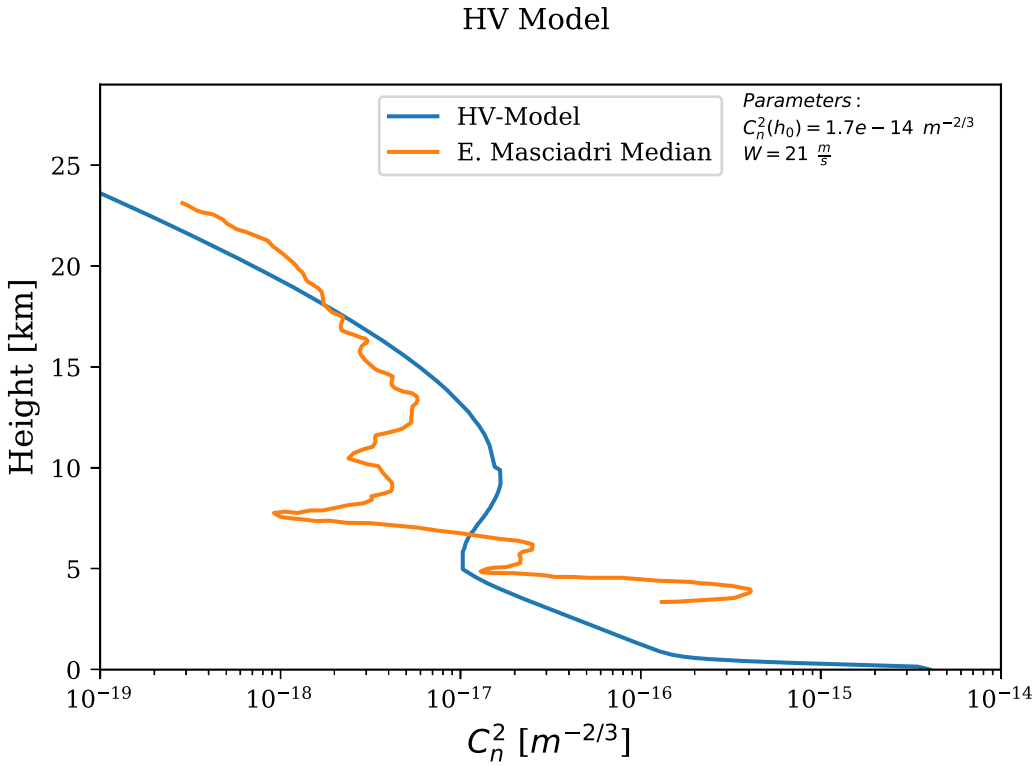

Figure 2.7: HV model computed with the parameters denoted in the right upper corner. Additionally the median profile from Mt. Graham measured by E. Masciadri is added for comparison [17].

The most widespread model is the HV model which is a modification of the Hufnagel-model by R. E. Hufnagel [20]. As he already pointed out himself, it is only valid above the first strong inversion layer, leaving a gap between the ground and the height of this first layer. To close this gap, the model was modified by Ulrich [25] following a suggestion of Valley [26], by adding a term at the end of the Hufnagel-model to take into account the atmospheric boundary layer, making it the Hufnagel-Valley model, which is described by equation (2.18).

$$C_n^2(h) = 0.00594 \cdot \left(\frac{W}{27}\right)^2 \cdot (h \cdot 10^{-5})^{10} \cdot e^{\frac{-h}{1000}} \cdot +2.7 \cdot 10^{-16} \cdot e^{\frac{-h}{1500}} + C_n^2(h_0) \cdot e^{\frac{-h}{100}} \quad (2.18)$$

The height h is in meters above sea level, furthermore the model needs only two input Parameters: W which is representing the root mean square of Wind speed in the atmosphere over the 5-20 km range above ground level, and a $C_n^2(h_0)$ value at the ground. Setting the parameters $W = 21\frac{m}{s}, C_n^2(h_0) = 1.7 \cdot 10^{-14} m^{-2/3}$ defines the HV 5/7 model.
This specific model exhibits a coherence diameter of $r_0 = 0.05\,m$ and a isoplanatic angle of 7 μrad for $\lambda = 500\,nm$, which are typical values for astronomic night-time conditions. A representative example of this model was plotted with a python code and is shown in Figure 2.7.
It has to be noted, that this model is a median representation of the actual $C_n^2(h)$ values in the atmosphere derived from mid-latitude data assuming a low tropopause.
Additionally, the exponential decay in the first 3 km is widely believed not to be a realistic model of the boundary layer [22].

2.5.3 Hufnagel-Andrew-Phillips model (HAP)

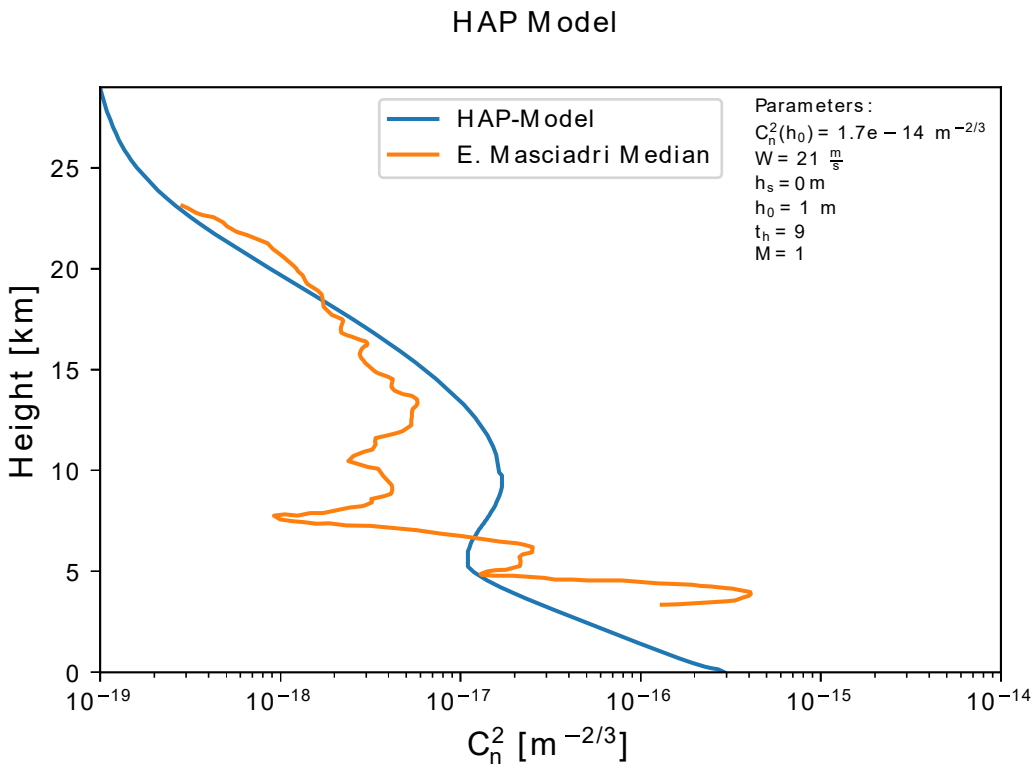

Figure 2.8: HAP model computed with the parameters denoted in the right upper corner. Additionally the median profile from Mt. Graham measured by E. Masciadri is added for comparison [17].

One modification of equation (2.18) is given by equation (2.19) developed by Andrew and Phillips to improve modelling of the refractive index structure parameter in the atmospheric boundary layer by adding the last term.
They tested their modified model with measurements during the day and found that their

term is a better representation than the term used by the Hufnagel-Valley model.

$$C_n^2(h) = M\left[0.00594 \cdot \left(\frac{W}{27}\right)^2 \cdot ((h+h_s)\cdot 10^{-5})^{10} \cdot e^{\frac{-(h+h_s)}{1000}} \cdot +2.7 \cdot 10^{-16} \cdot e^{\frac{-(h+h_s)}{1500}}\right] + C_n^2(h_0) \cdot \left(\frac{h_0}{h}\right)^p \tag{2.19}$$

$$p = \begin{cases} -0.11 \cdot (12-t_h)^2 + 1.83 \cdot (12-t_h) - 6.22 \;\; if \;\; 0.75 < t_h < 3.5 & \text{(2.20a)} \\ 1.45 - 0.02 \cdot (t_h - 6)^2 \;\; if \;\; 3.5 < t_h < 8.5 & \text{(2.20b)} \\ -0.048 \cdot {t_h}^2 + 0.68 \cdot t_h - 1.06 \;\; if \;\; 8.5 < t_h < 11.25 & \text{(2.20c)} \end{cases}$$

$$t_h = \frac{TIME - SUNRISE}{t_p} \tag{2.21}$$

$$t_p = \frac{SUNSET - SUNRISE}{12} \tag{2.22}$$

It has to be noted that the models are similar above the inversion layer where the atmospheric boundary layer ends.
Beside the parameters W and $C_n^2(h_0)$ the HAP model has the additional parameters h_s, h_0, t_h and M.
h_S represents the elevation of the laser site above sea level in meters, h_0 is the height over ground in meters used to measure the reference value $C_n^2(h_0)$. M represents a scaling parameter to adjust the HAP-model to different measured or estimated values, p is calculated based on the time of the day to represent stable or unstable conditions which occur during a day. According to [3] p is calculated for one specific site, namely the Hollister Airport in California, USA. To do so the time between sunrise and sunset is split into twelve parts and the temporal hour t_h is calculated based on this timespan and the current delta to sunrise.
Since this calculation has to be changed for different locations, the p usually assumes a constant value of $\frac{4}{3}$ for any further calculations. Figure 2.8 shows one calculated atmospheric profile.

2.5.4 US army research laboratory model (ARL)

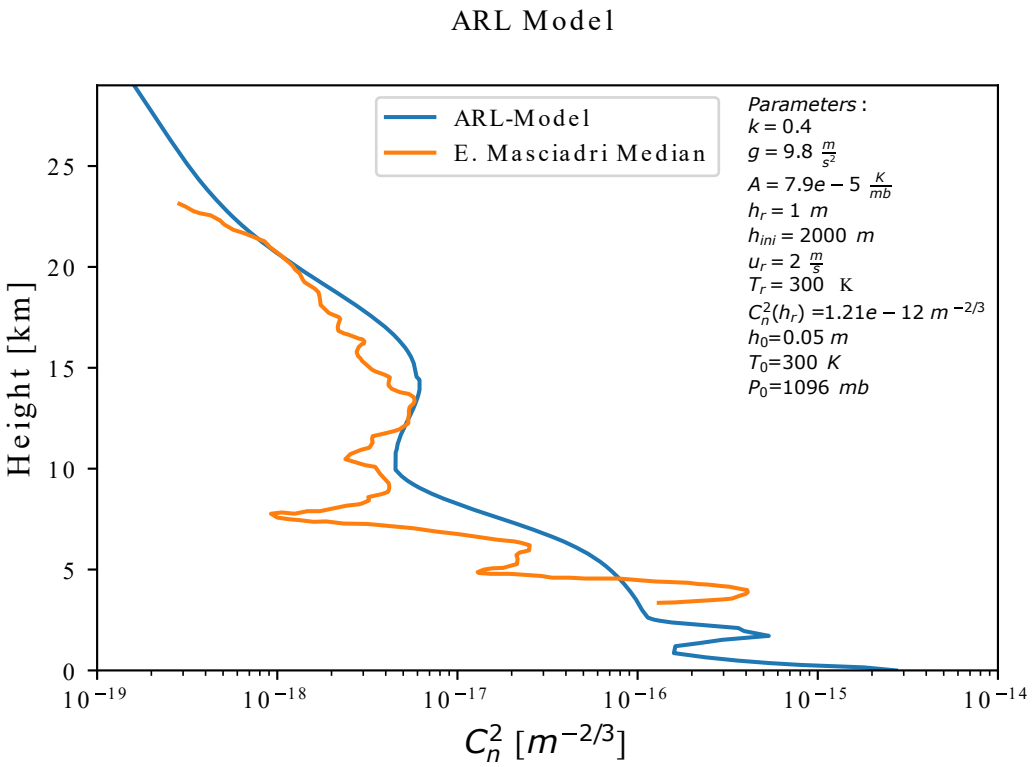

Figure 2.9: ARL model computed with the parameters denoted in the right upper corner. Additionally the median profile from Mt.Graham measured by E.Masciadri is added for comparison[17].

This model developed in 2006 by Tofsted et al. [8] assumes the atmosphere to be divided into three different layers, in order to use different other models and connect them to get one single equation describing the $C_n^2(h)$ function.
The first layer is the surface layer ranging from the ground to approximately 100 m, followed by the convective boundary layer and concluding with the free atmosphere which is modelled with the CLEAR I atmospheric model.
The model was implemented utilizing the equations (43C), (44), (45), (46), (47), (20), (29) and the temperature and pressure distribution from the report[8]. An exemplaric result is shown in figure 2.9, with the parameters used presented as well. Compared to the other two models the ARL model depends on a multitude of parameters which are listed below [6].

- Dimensionless von Karman constant : k_{karman}
- Gravitational acceleration: g
- Dry-Air wavelength-dependence function for 500μm [22]: A
- Reference height: h_r
- Height of the elevated inversion base : h_{ini}
- Average wind speed: u_r
- Reference temperature: T_r

- Reference structure coefficient: $C_n^2(h_r)$
- Roughness height: h_0
- Temperature at reference level: T_0
- Pressure at reference level: P_0

This adds considerably to the complexity but also to the flexibility of the ARL model. Since this model needs more parameters than the other ones and also needs measurements to calculate theses parameters it is not as widespread as the other two models. In the course of this thesis it was also not used apart from demonstrating the similarities of the laser profile in section 4.6.

3 Modelling

Since the wave-optical propagation in the turbulent atmosphere is a complex topic, one has to consider a multitude of effects and their connections, as can be seen by the previous chapter. To be able to understand how a laser beam propagated from the ground to a satellite is influencing it, the parameters of the laser arriving at the target have to be known. Without this knowledge it is impossible to design a laser optical system for post mission disposal.
Beside understanding the underlying theory a model has to be developed to enable engineers to estimate important design parameters like the beam diameter, or the intensity distribution at the target.
In this thesis different modelling approaches are compared, and the existing tool AtmProp is supplemented with a turbulence model which accounts for the fact that the refractive-index turbulence in the earths atmosphere is a function of the height above ground.
In this chapter two different approaches to model the wave-optical propagation are presented as well as a python program developed to conduct multiple simulations.
The two models are a numerical one implemented in the tool AtmProp in section 3.1, and a analytical one presented in section 3.2.

3.1 Atmospheric propagation tool

The software called AtmProp in the course of this thesis is a tool for the "Atmospheric Propagation" of laser beams developed at the DLR institute for technical physics. It's a numeric code written in fortran due to its needs regarding computational performance.
The principle of AtmProp is to split up the propagation path into a number n of segments of a length Δz_j between positions z_j.
Each step z_j has one assigned value of C_n^2 given by the parameter file. This value is used to calculate a phase distortion in terms of a phase screen, placed in the middle of the segment, at $z_j + \frac{\Delta z_j}{2}$, according to equation (3.1).
This phase screen has no spatial extent, but is rather a representation of the phase distortion experienced by a laser beam travelling the whole distance Δz_j, combined into one phase screen which is distorting the wave once it passes its position. Summed up the initial wave given by the parameter file is calculated at z_0, propagated in vacuum till $z_0 + \frac{\Delta z_0}{2}$ where the phase screen is modifying the phase of the incoming wave. The modified wave is further propagated through vacuum to z_1, where it is used as new input wave and the same process is repeated.

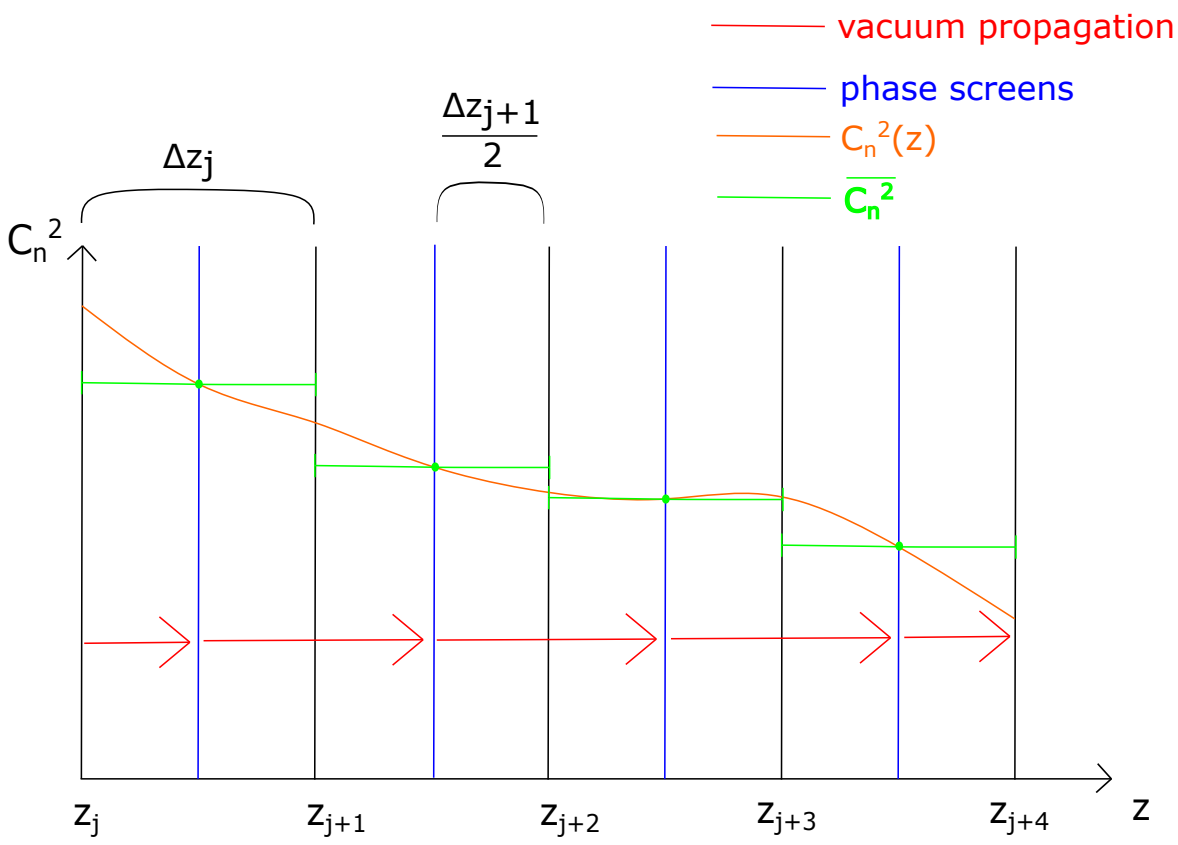

Figure 3.1: Schematic of the discretization used in AtmProp

Figure 3.1 is showing the scheme of discretization and how the single steps are calculated for an exemple case. This case is going from z_j to z_{j+4} the single steps shown in black with the phase screens in blue in between. Furthermore, the averaged C_n^2 are shown in bright green, while the "actual" course of $C_n^2(z)$ is drawn in orange. The red arrows are showing the vacuum propagations calculated by AtmProp.
To calculate the impact of a phase screen according to Fleck, let $E_j(x,y)$ be the solution of (2.14) arriving at z_j, the solution arriving at z_{j+1} is [13]:

$$E_{j+1} = e^{-\frac{i}{4k}\Delta z_j \nabla^2} \cdot e^{-ik\Gamma} \cdot e^{-\frac{i}{4k}\Delta z_j \nabla^2} \cdot E_j \tag{3.1}$$

Following Fleck the phase shift Γ to solve equation (3.1) is calculated by [13]:

$$\begin{aligned}\Gamma(l_x\Delta x, l_y\Delta y) = \frac{2\pi}{N}\left(\frac{0.033\pi\Delta z C_n^2}{\Delta x\Delta y}\right)^{\frac{1}{2}} \cdot \\ \sum_{n_x=-\frac{N}{2}+1}^{\frac{N}{2}} \sum_{n_y=-\frac{N}{2}+1}^{\frac{N}{2}} \frac{e^{\left(i\pi\frac{n_x l_x}{N} + i\pi\frac{n_y l_y}{N}\right)}}{\left[\left(\frac{2\pi L}{L_0}\right)^2 + \frac{2\pi {n_y}^2}{N} + \frac{\pi {n_y}^2}{N}\right]^{\frac{11}{12}}} \cdot \\ \left[a'(n_x,n_y) + ia''(n_x,n_y)\right]\end{aligned} \tag{3.2}$$

Equation (3.2) is the result of starting with (2.16) and inserting equation (2.17) to connect the refractive index fluctuations with the Karman power spectrum written in equation (2.12). The statistical nature of δn is taken into consideration while calculating the phase change

$\Gamma_{turb}(x,y)$ with a Monte Carlo technique[13].
Regarding the propagation steps in vacuum, equation (2.13) is simplified by removing the term $k^2\delta\epsilon E$. The resulting equation is used to find the solution after the according propagation distances.
After arriving at the end of the simulation by repeating the described procedure till z_{end}, the simulation can either be finished and the results outputted or to account for the stochastic nature of the problem the same calculation can be repeated and the result can be averaged with the result beforehand. The number the same propagation is conducted can be choosen by adjusting the number of runs in the parameter file. Each calculation from the beginning till the end is called a run, in the end AtmProp is averaging all results from all runs. For a more detailed description of the methods implemented in AtmProp, the reader should consult Fleck [13].
After finishing the propagation AtmProp is outputting a number of files which can be used to analyse and compare the numeric results to other models and to draw conclusions from these results.
For this thesis the averaged intensity distribution at the final screen and the file containing twelve parameters of a specific run are utilized.
This files are collected by the developed software "PropRunner" which is a python based set of modules to run simulations and to enable the user to input different turbulence models regarding the height distribution of the C_n^2 values.
As a result from this calculating principle the python code developed to create input files from different turbulence distribution models had to consider this structure by giving one value for the structure function as well as the distances between the different height levels. The creation of this files is explained in the following section.

3.1.1 Influence of the calculation area

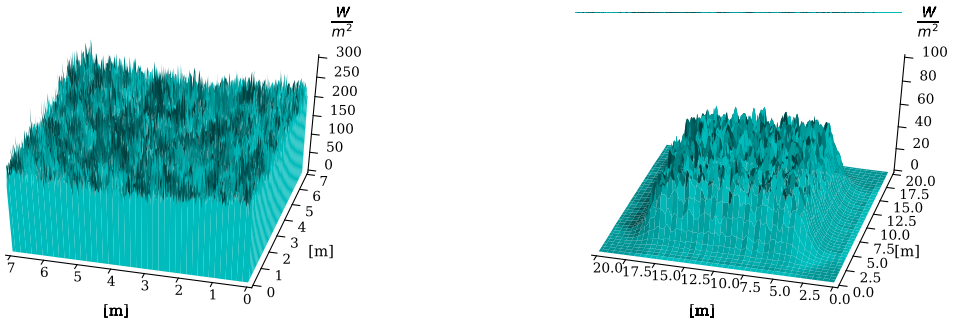

(a) Example of the calculation diameter choosen to small for the beam size and the turbulence strength.

(b) Example of the calculation diameter choosen to big and hence the fourier space being too small for the beam size and the turbulence strength.

Figure 3.2: Two examples for using AtmProp with the wrong parameters

One issue arising from the the fourier transformations in AtmProp is a conflict of interest arising from the fact that increasing the size of the physical space is decreasing the size of the fourier space.
With increasing level of turbulence the beam starts to spread more and more over the calculation area. The further the beam is spread the bigger the physical space has to be chosen which is decreasing the fourier space which exhibts the property of being periodical.
A complete theoretical evaluation of this errors is out of the scope of this thesis and therefore the signs of choosing an inappropriate diameter for the calculated field are briefly presented, for the case of setting the physical space too small as well as setting the fourier space too small.
Choosing the physical space too small results in power of the beam to be lost, hence the beam has less power at the end of the propagation than it had at the initial step. Additionally, to this the beam starts to have a high signal to noise ratio.
Solving this issue by simply raising the calculation radius is possible but might result in the fourier space getting too small, resulting in a beam which is limited to a rectangular area inside the calculation area.The fourierspace becomes visible in the real space in the intensity distribution, as shown in figure 3.2b. In addition the intensity flats out due to the parts of the intensity which are reflected to the wrong position and interfering with the intensity around their new position.
Both spaces have to be chosen sufficiently large to prevent both phenomena from happening, because otherwise the errors introduced to the results of the simulations become too high rendering them wrong and therefore useless.

3.2 Analytical modelling

Beside the numerical modelling and the calculations done with AtmProp some analytical formulae also exist to describe the wave-optical propagation of laser beams in the atmosphere. In case of assuming a gaussian beam shape it is possible to derive analytical equations to calculate certain properties, for instance the beam radius $w(z_{propdir})$ as a function of the distance

along the propagation direction $z_{propdir}$ as written in equation (3.3), which is considering propagation in vacuum.
The relevant parameters here are the beam propagation parameter M^2, the laser wavelength λ in $[m]$, the distance from the telescope's exit $z_{propdir}$ in $[m]$, the initial 2^{nd} moment beam radius at the telescopes exit w_{init} in $[m]$ and the focal distance f in $[m]$ of the telescope. This focal distance equals the geometrical optical focus but not the wave-optical focus.

$$w^2_{vacuum}(z_{propdir}) = \left(\frac{M^2 \cdot \lambda \cdot z_{propdir}}{\pi \cdot w_{init}}\right)^2 + w^2_{init} \cdot \left(1 - \frac{z_{propdir}}{f}\right)^2 \tag{3.3}$$

In the following it is assumed that the telescope used has no pointing error, hence the formulae shown here are without taking any pointing error into account.
Equation (3.3) is limited to the case of a beam propagating through vacuum. In the case of propagating through atmospheric turbulence there are also equations for a gaussian beam derived by, e.g. Belmonte [4], Fante [11] and Dios [9].
These formulae are taking the effect of turbulence into account using an integrated value called coherence diameter r_0 in $[m]$. This paramter is added to equation (3.3) which leads to equation (3.4):

$$w^2_{analytic}(z_{propdir}) = \left(\frac{M^2 \cdot \lambda \cdot z_{propdir}}{\pi \cdot w_{init}}\right)^2 + w^2_{init} \cdot \left(1 - \frac{z_{propdir}}{f}\right)^2 + 8 \cdot \left(\frac{\lambda \cdot z_{propdir}}{\pi \cdot r_0}\right)^2 \tag{3.4}$$

Since atmospheric turbulence is a function of the height above a reference level the coherence diameter is calculated through integrating over the relevant atmospheric layers for the specific propagation problem with equation (3.5), $k = \frac{2 \cdot \pi}{\lambda}$ and the zenith angle ζ [4] [9] [11].
H in $[m]$ is the height till which the propagation is taking place, $\xi_H = \frac{h}{H}$ with h being the height above a reference height where a C_n^2 value is given.
This transformation is the reason that the integral in equation (3.5) is integrated from 0 to 1.

$$r_0 = \left(0.42k^2 \cdot sec(\zeta) \cdot H \int_0^1 (1 - \xi_H)^{\frac{5}{3}} \cdot C_n^2(\xi_H \cdot H) d\xi_H\right)^{-\frac{3}{5}} \tag{3.5}$$

The coherence diameter is the sphere over which the phase variance is exactly π. It decreases with increasing turbulence strength.
. Or to express it in a more accessible way, two points on the x-y plane are getting incoherent if they are more than r_0 apart from each other.
In this thesis the integral from equation (3.5) is calculated with the numpy package and the function numpy.simps. This function is using a simpson method for the calculation, the parameter "even" has been set to "first", due to the fact modelling with the simpson rule is done till the end of the curve where a trapezodial rule is applied to average the last interval.
With the equations written above a gaussian laser beam can be propagated in a wave-optical way similar to the simulations with AtmProp.
The interesting question to ask here is in how far the results from the two ways to model the wave-optical propagation of laser beams in the atmosphere with the influence of atmospheric turbulence are comparing to each other. For the comparison between the analytical and the numerical model the same C_n^2 distributions have been used, one time to propagate from step to step, the other time to calculate the coherence diameter r_0.
In chapter 4 specific problems are calculated with the analytical and the numerical model. After conducting these simulations the results are compared to each other, to investigate the differences between both models.

3.3 Python code

In order to supplement and use the AtmProp software a number of modules and programs have been developed which are named "PropRunner" in the following sections.
The central module is called PropRunner.py and it is calling all other functions and modules including AtmProp itself.

3.3.1 Input files

Three Input files specifying the parameters of each case are needed:

- AtmPropexample.par : An exemplary parameter file to be modified for each individual case
- CaseList.txt : A list of four parameters to be varied and a list of "fixed" parameters.
- Turbulencemodel.txt: All parameters needed to use a specific turbulence model for a $C_n^2(h)$ distribution.

The **AtmPropexample** file determines all parameters which can be used as input for runs of Atmprop. In addition it is also the starting point for PropRunner since it is the template which is edited to create the parameter files used in all cases. The following parameters are given in this template:

- ComputationRadius in [cm]
- Sampling [-]
- Runs [-]
- ContinuePrevious [-]
- UseAperture [cm]
- AnnularInner [cm]
- AnnularOuter [cm]
- InitialSchellRadius [cm]
- NumberLayers [-]
- Overshoot [-]
- InitialPower [W]
- InitialRadius [cm]
- InitialSG [-]
- Wavelength [nm]
- InitialROC [m]
- UseTurbulence [-]
- Cn2 [$m^{-2/3}$]
- Distance [m]
- Substeps [-]
- InnerScale [mm]
- OuterScale [m]
- SeedByClock [-]
- UseLargeScreen [-]
- OuterScreens [-]
- TurbulenceModel [-]

- Elevationcorrection [-]
- Elevationangle [grad]
- PropagationDistance [m]
- UseThermBlooming [-]
- AersolAbs $[Mm^{-1}]$
- Velocity [m/s]
- VelAngle [deg]
- RefrIdx [-]
- MassDensity $[kg/m^3]$
- Pressure [hPa]
- IsobHeatCap $[\frac{kJ}{kg.K}]$
- IsocHeatCap $[\frac{kJ}{kg.K}]$
- Buckets [-]

The parameters "Cn2", "Distance" and "Substeps" can be filled with a list of parameters to enable a propagation over different segments, with different lengths and different C_n^2 values. It has to be noted that all three lists need to share the same number of entries. In case they do not AtmProp is exiting with an error.
Supplementing this is the **CaseList** file which is giving the user the ability to specify four of the parameters mentioned above to be varied. **CaseList** takes also lists as possible input for each of the four chosen parameters. PropRunner is combining all different values of this four parameters to determine the number of cases to be calculated.
To illustrate this lets assume that each of the four parameters consists of a list of five entries. Therefore the number of cases becomes: $n_C = 5 \cdot 5 \cdot 5 \cdot 5 = 625$. In addition to this four parameters, there is also a number of parameters called "Fixed parameters" which are set the same for all cases, meaning that all parameter files for one experiment will exhibit the same value for this fixed parameters.
The last file needed is **Turbulencemodel.txt** which has the input parameters for each single turbulence model and which forms the basis to calculate the values of $C_n^2(h)$. Since each model is different the amount of paramters and the kind of parameters differs for each model. The parameters relevant for each model are presented in the previous sections where the available models are presented.
Beside this files three more parameters are needed for starting a simulation, the path to the folder containing the inputfiles, the name of the specific casefile file to be used and the name of the experiment to identify the run later.

3.3.2 Python modules

With all this inputs given, the programm first calls createtree.py in order to establish how many cases have to be calculated and to create the folder structure with one folder per case. Also the parameter files are created from the list of turbulence values for each propagation and the propagational distances Δz_j.
To write the turbulence models into the parameter files, the module Writeparfile.py is called which collects the parameters needed to calculate the turbulence distribution and calls the module CalcCn2.py where the calculation of the C_n^2 values is taking place.
The CalcCn2 module is calling the modules for all three turbulence models, and hands over the final lists for the propagation distance and the according values for C_n^2 to Writeparfile which writes them into the parameterfile.

Once this is done AtmProp is called in the path where the parameterfile is so the results are also written in the same casefolder. At the end of the simulation createtree.getfiles() is copying the relevant files from these results into one folder so they can be accessed by the postprocessing routines more easily. The results are then used to calculate all relevant data and graphs needed to evaluate the experiment. Figure 3.3 is showing the structure of PropRunner as a flow diagram, the modules are marked as green tilted rectangles, the most important processes are shown with brown rectangles.

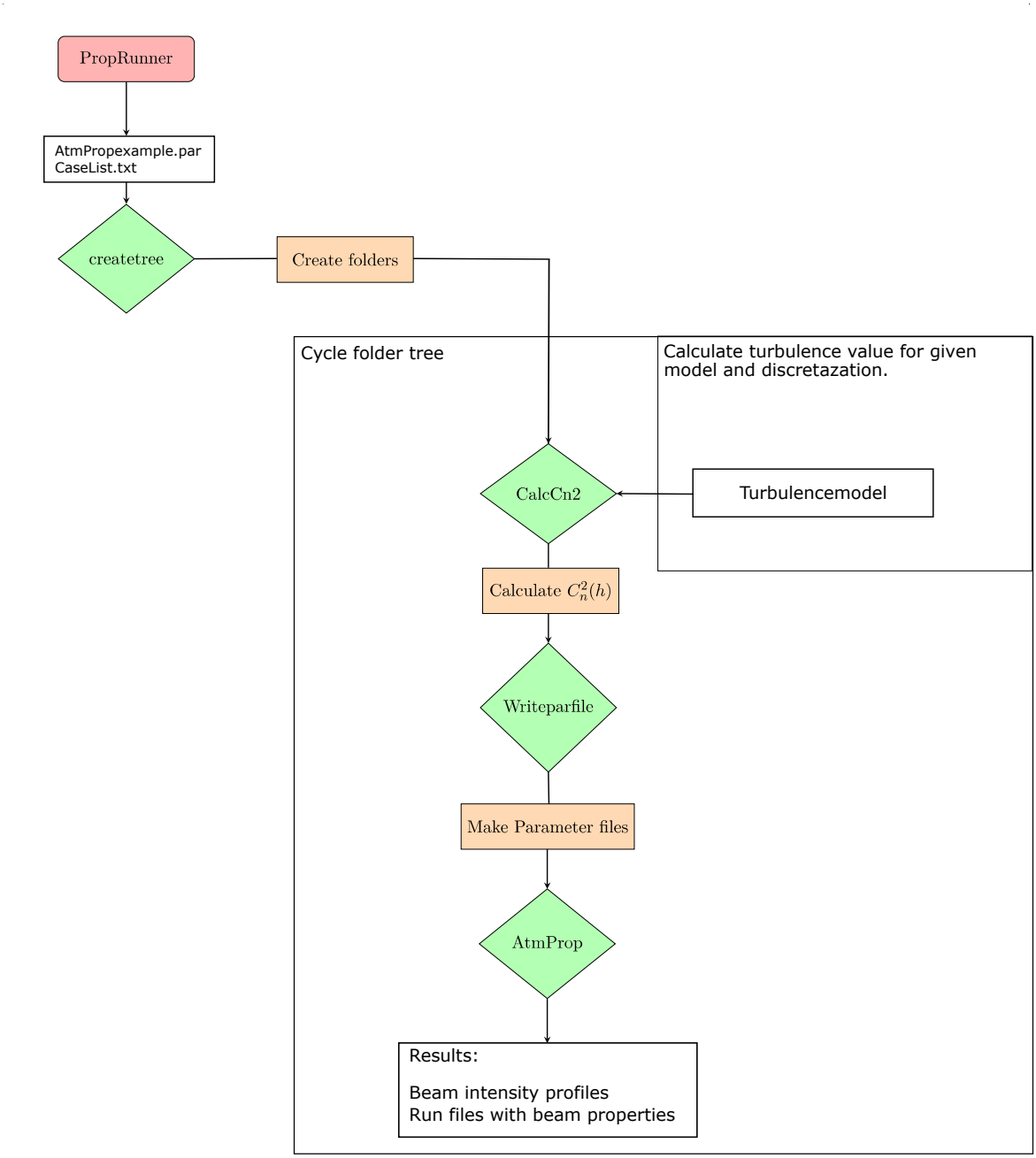

Figure 3.3: Flow diagram of PropRunner

3.3.3 Numerical reconstruction

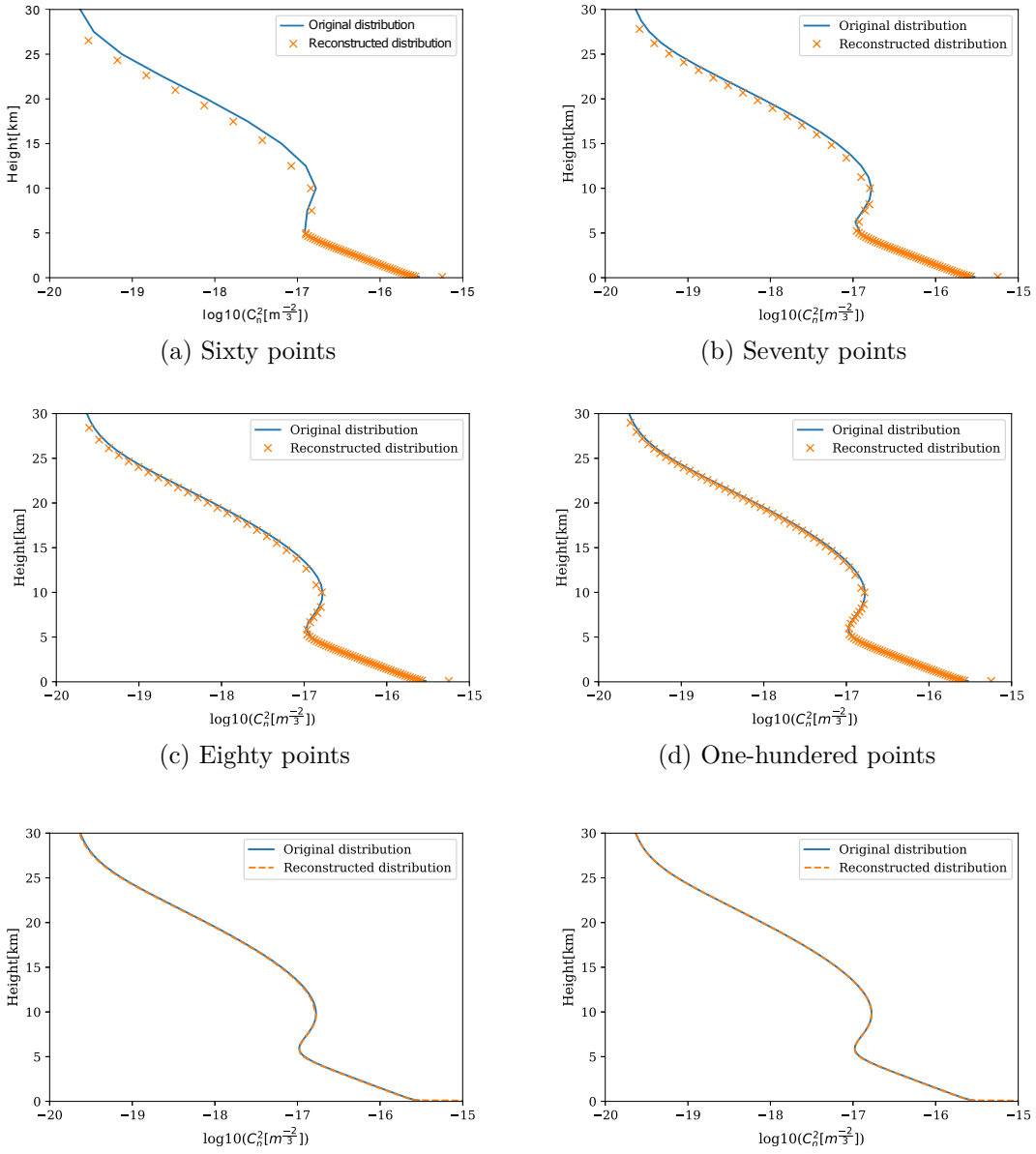

(a) Sixty points

(b) Seventy points

(c) Eighty points

(d) One-hundered points

(e) Two-hunderd points

(f) One-thousand points

Figure 3.4: The numeric reconstruction with different number of points showing the reducing difference between the function and the used results with increasing number of points.

The available models for calculating $C_n^2(h)$ are giving a result as a function of height, but they are not all easily converted to a function of the form $h(C_n^2)$. Therefore the way to compute the distribution of C_n^2 is starting with generating a list of height values which are distributed from zero to 30 km with equal distance.
Additionally the lower layers of the atmosphere are more important for the propagation they are resolved with a higher resolution in this thesis.
The resulting values of C_n^2 are discretized with a constant with varying distance between each other which makes the single steps quite different regarding the turbulent impact on the beam

even though they are equally spaced regarding height.
Since this is impairing the comparability a constant spacing is desired regarding the C_n^2 values. The issue arising here is the values of C_n^2 are at the order of magnitude between 10^{-12} and 10^{-22} which is small and making the computation costly. As a consequence the logarithmic values of C_n^2 are used and the distribution is converted to one where the C_n^2 values are equally spaced in the log10 space.
To realize this a program was created which is part of the PropRunner software developed in the course of this thesis. The single steps of this program are described in the following.

First step

The module to realize the conversion described in the section before was developed to obtain a regular grid with equally space height values.
The C_n^2 values are calculated according to the desired turbulence model with the parameters given in the according input file, the number of given steps u in this file is determining the dimension of the resulting lists.
Resulting from this are two lists of the dimension u, one of them is containing the height values h_0 to h_u with constant spacing and the other one is containing the log10 $C_n^2(h_0)$ to log10 $^2_n(h_u)$ values in the log10 space. To simplify notation we define $l_n^2 = log10(C_n^2)$. Interpreting this values as discrete function of the form $l_n^2(h)$ a slope can be defined for $\frac{\partial l_n^2(h)}{\partial h}$. This derivative can take the values $\frac{\partial l_n^2(h)}{\partial h} < 0$ or $\frac{\partial l_n^2(h)}{\partial h} > 0$.
This is used to split up the lists into segments at the points where $\frac{\partial l_n^2(h)}{\partial h}$ is switching its sign. The number of segments is usually small, for instance in the HAP model which was mainly used in this thesis the list is split into three different parts.
For each of this parts the following operations are conducted and the results of each calculation are concatenated afterwards.

Second step

The next step is to calculate the difference between the maximum value of l_n^2 and the minimum value of l_n^2 for the current segment.
This interval is used to create a list of equally spaced l_n^2 values spanning from the maximum l_n^2 to the minimum l_n^2 with u being the number of values the old equally spaced height array exhibited, and also the number of values for the new list.
This list is now equally spaced regarding l_n^2 values, in the following called L_n^2. For each entry L_n^2 the difference to each value $l_n^2(h_j)$ is determined to get the index j_{min} where this difference is at a minimum. With this index an interval from $h_{j_{min-1}}$ to $h_{j_{min+1}}$ is defined which is split into one-hundred entries with the index q, hence a list going from $h_{j_{min-1}}$ to $h_{j_{min+1}}$ with the spacing $\frac{h_{j_{min-1}} - h_{j_{min+1}}}{100}$. The values of this list will be called h_q^I for now.

Third step

Next each element of this list is used to calculate a $l_n^2(h_q^I)$ value. After calculating all one-hundred values the index q_{min} of the minimum difference between L_n^2 and $l_n^2(h_q^I)$ is searched. The resulting $h_{q_{min}}^I$ is the height result fitting to the L_n^2 value: h_j. After repeating this for

each entry of L_n^2 and converting from log10 space back into C_n^2-space two lists are available: L_n^2 and $h_j(L_n^2)$, with u entries.

Example of reconstruction

Since the process of numerical reconstruction is quite complex, one example is presented here to clarify the way it is working. Figure 3.5 is showing an example of $l_n^2(h)$ and a according list of h with a constant spacing of 2500 m.
To understand the process one must begin in the left upper corner where start is written. The list of $l_n^2(h_u)$ values ranges from -16.8994 to -19.7067, following the orange and the blue arrow from there one arrives at the L_n^2 list where with a spacing of 0.3509 the list is filled with nine values.
The steps are repeated for each index going from 0-u, but are shown here for the index four as an example. Therefore a value $h(l_n^2)$ is searched for $L_{n_{needed}}^2 = -18.3031$, which is surrounded by a green line. Going back the starting list $l_n^2(h_u)$ one needs to figure out the height intervall the desired result is in. This is found by getting the index of the entry of $l_n^2(h_j)$ where the difference to $L_{n_{needed}}^2 = -18.3031$ is minimal which is the case for the index three.
This is expanded by one in each direction defining the lower limit of the height list $h_{j_{min-1}} = 17500\,m$ and the upper limit $h_{j_{min+1}} = 22500\,m$. Between this limits a list of height values is spanned, in contrast to the implemented one only ten are used here to simplify the calculation. Next all values $l_n^2(h_q^I)$ are calculated and compared to $L_{n_{needed}}^2 = -18.3031$ by computing the difference from each entry to $L_{n_{needed}}^2$.The minimum is found at the Index six, so the resulting value has been found. Its the entry six of the list h_q^I with $h_6^I = 20833.3\,m$, and written to the result list $h_j(l_n^2)$ at index four.
For each entry this method is conducted till $h_j(L_n^2)$ is filled with heights which have corresponding L_n^2 values with an approximately equal spacing in log10 C_n^2-space.

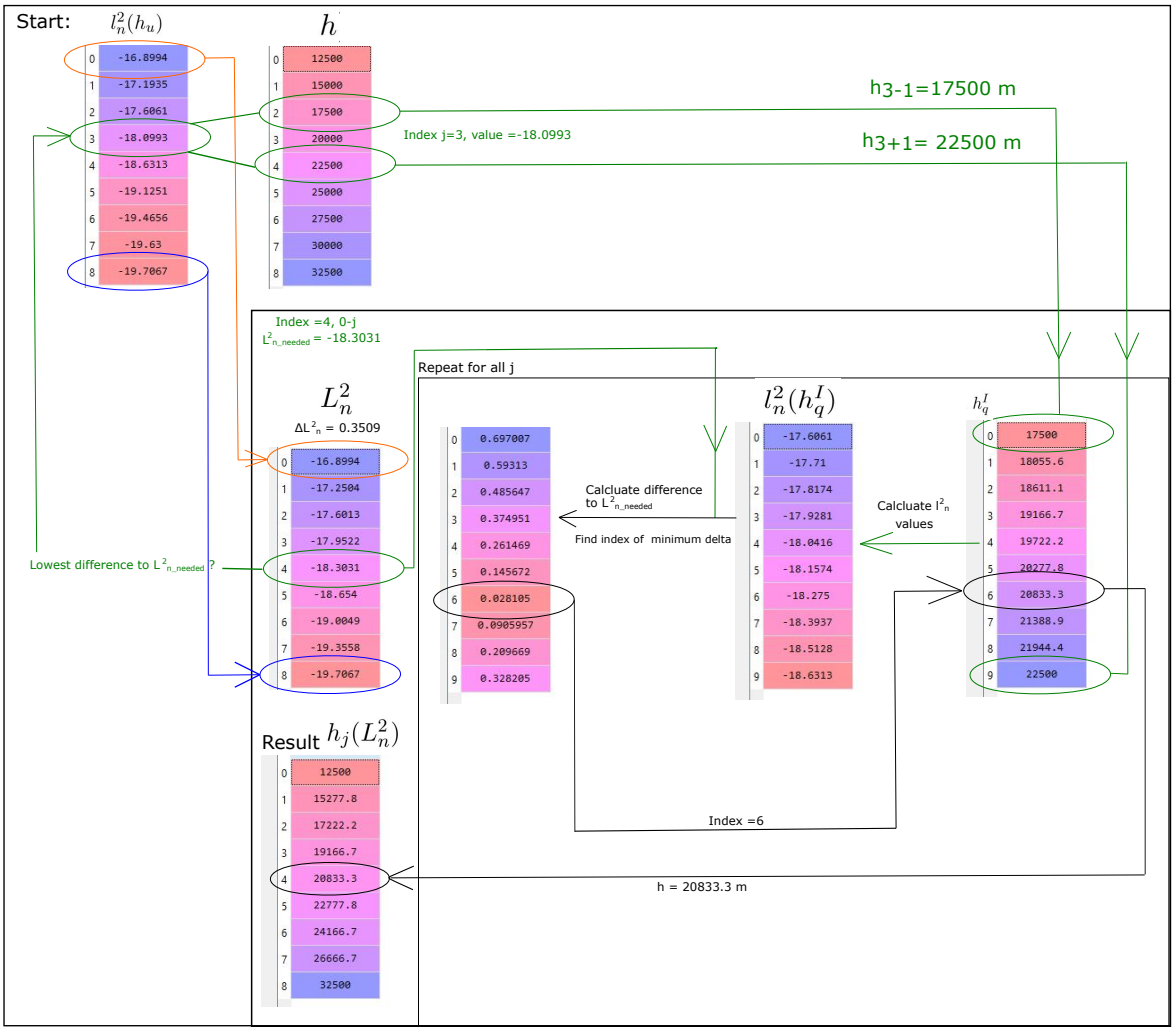

Figure 3.5: Example of numerical reconstruction with nine points for the distribution and ten points for the h_q^I grid.

Results of the calculation

Figure 3.4 shows the final result of this calculation with six sub figures.
These calculations are shown for a HAP model since this model was mainly used for the simulations in this thesis. The number of points used to calculate the ${}^{eq}_{u}C_n^2(h_u)$ function as well as the reconstruction of $h_j({}_jC_n^2)$ is increased from sixty points (3.4a) to one-thousand (3.4f). The blue line is representing the ${}^{eq}_{u}C_n^2(h_u)$ values which is also looking angular due for low number of points.The orange x-symbols are representing the values of $h_j({}_jC_n^2)$, till 200 points for which a dashed line is used. For the lower 5 km the resolution is reduced since this values are more important than the upper layers. One result of this is that the number of points in the upper 25 km is even further reduced resulting in only ten points used above 5 km, in the case using only sixty points for the calculation. The two curves are showing, that for a low resolution the agreement is fairly low but increasing to a high level after reaching one-hundred points, and even increasing when the resolution is set to one-thousand points.
This shows that the reconstruction is working precisely and can be used for the further calculations in this thesis.

3.3.4 Verify r_0 calculation

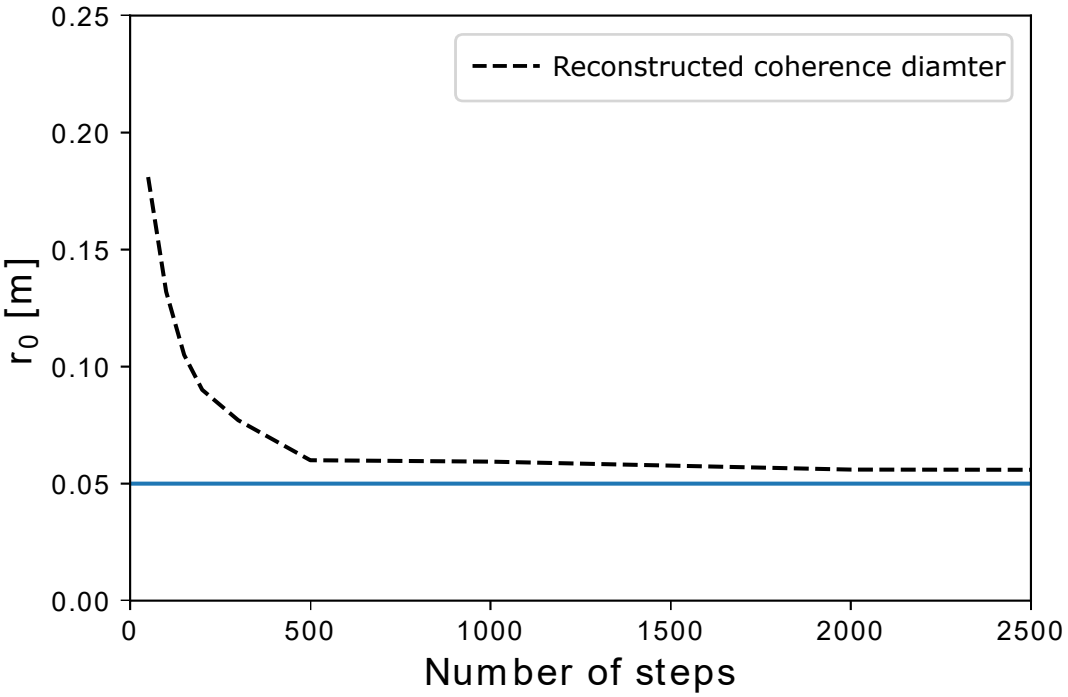

Figure 3.6: Coherence diameter of the HV 5-7 model after reconstruction with different number of steps and for $\lambda_{laser} = 500nm$.

The analytical models presented in this thesis need one integrated parameter in order to not having to deal with a whole list of parameters as explained in the sections beforehand.
To make sure that the analytic models and the numeric models are compared with the same turbulence condition the resulting distribution for C_n^2 used in the numeric simulation is read from the parameter file of the according case.
Next equation (3.5) is used to calculate the coherence diameter which has to be used for calculating analytic results in this specific case.
In literature dealing with the impact of atmospheric turbulence on laser beams quite often the Hufnagel-Valey 5-7 model is mentioned, which is also presented here.The condition which arises here is that the implementation of this model has to have a coherence diameter of $r_0 = 5cm$, which was checked to clarify that the model is working properly.
An important issue here is the fact that the resulting C_n^2 values from the turbulence models have been calculated to be equally distributed regarding the log10 space and therefore the resolution of this reconstruction becomes important.
To see if the calculation of the coherence diameter is correct the resolution of a given Hufnagel-Valley 5-7 model was increased step by step and the resulting coherence diameter has been calculated. The results are shown in figure 3.6, the blue line in figure 3.6 is showing the 5 cm coherence diameter found in literature.The calculated r_0 is plotted over the number of steps which have been used to calculate the $C_n^2(h)$ distribution of the HV-model.It can be seen that the value of r_0 is converging to the value found in literature for a increasing number of steps. One important thing to note here that as long as the used turbulence discretization for the analytical and the numerical calculations is the same, they can be compared.

4 Simulations and results

After presenting the two different ways of modelling,the next step is the comparison of results for the propagation calculations. The analytical model and the numerical model presented beforehand, used with AtmProp and PropRunner are compared in different Experiments.
First a very simple gaussian beam propagating without the influence of atmospheric turbulence is calculated. Because the beam is analysed here without the influence of a telescope a set of formulae only containing parameters of the propagating wave are used in section 4.1.

4.1 Gaussian beam verification

4.1.1 Analytical solution

In order to create a reference for future users, the propagation properties of a reference beam with a gaussian profile was simulated with the program AtmProp as well as solved analytically. This serves to provide a fundamental proof of AtmProp's capability to solve the wave-optical propagation problem.
One convenient attribute of a gaussian beam is that it's possible to calculate the beam properties along the whole propagation axis in an analytical way.
The following formulas give the radius of curvature R(z) of the wave front (4.1), the beam radius w(z) with z = 0 assumed to be at the beam waist (4.2)and the Rayleigh range z_0 (4.3)[12].

$$R(z_{wave}) = z_0 \left[\frac{z_{wave}}{z_0} + \frac{z_0}{z_{wave}} \right] \tag{4.1}$$

$$w(z_{wave}) = w_0 \sqrt{1 + \left(\frac{z_{wave}}{z_0} \right)^2} \tag{4.2}$$

$$z_0 = \frac{\pi {w_0}^2}{\lambda} \tag{4.3}$$

Equation (4.2) differs from equation (3.3), only in the choice of boundary conditions. Equation (3.3) takes a system-centered perspective with the location (z=0), and the radius of curvature of the sending telescope as input parameters. In contrast, equation (4.2) presents a beam-centered perspective which gives the beam parameters w(z) and R(z) as a function of the distance from the beam waist.
Furthermore equation (3.3) is not using beam parameters but rather parameters of the sending telescope.
The three equations above are solved for z_0 by solving equation (4.3) for w_0 and inserting it into equation (4.2) and replacing the unknown variable z by the solution of (4.1) solved for z, which results in the following equation:

$$w(R) = \sqrt{\frac{\lambda \cdot z_0}{\pi}} \cdot \sqrt{\frac{R^2}{2 \cdot {z_0}^2} + \frac{R}{z_0^2} \sqrt{\left(\frac{R}{2} \right)^2 - z_0^2}} \tag{4.4}$$

With knowledge of the beam-radius and the curvature of the wave at one single coordina=te z, equation (4.4) can be solved for the unknown variable z_0, which enables the calculation of the beam waist radius using equation (4.3).
In case it is desired, the position of the wave-optical focus can be calculated as well solving equation (4.2).
It has to be noted that for this thesis the beam radius of gaussian beams is defined as the radial distance from beam centre at which the intensity dropped to $\frac{1}{e^2}$ its peak value.

4.1.2 Reference beam

In the context of the propagation of a laser beam through a random medium, the only position along the propagational axis where all parameters of the laser beam are known is the exit plane of the sending telescope. At this plane the laser beams profile can be fixed to start propagating with a specific profile like a gaussian beam. Along the propagation axis the beam will in general deviate from its initial form.
Therefore the attributes of the beam can only be defined at this position and for the following considerations in this section the $z = 0$ position is shifted from the beam waist to the sending telescope.
The Gaussian beam chosen for the verification has the following attributes in the telescope's exit plane, additionally the beam parameters z_0 and w_0 were calculated from the analytical expressions.

- Wavelength: $\lambda = 1030nm$
- Initial beam radius: w(0) = 0.5 m
- Radius of curvature of the wave front: R = 500 km
- Power of the laser beam: P = 10 kW
- Rayleigh range (Calculated with equation (4.4)): 229.3 km
- Minimum beam radius (Calculated with equation (4.3)): w_0= 0.274 m
- Turbulence usage: no
- Number of Runs: 1

The reference beam parameters have been chosen in view of the targeted usage scenario: Laser beam propagation to satellite orbits. Note that the reference beam defines an optimum case without turbulence.

4.1.3 Results

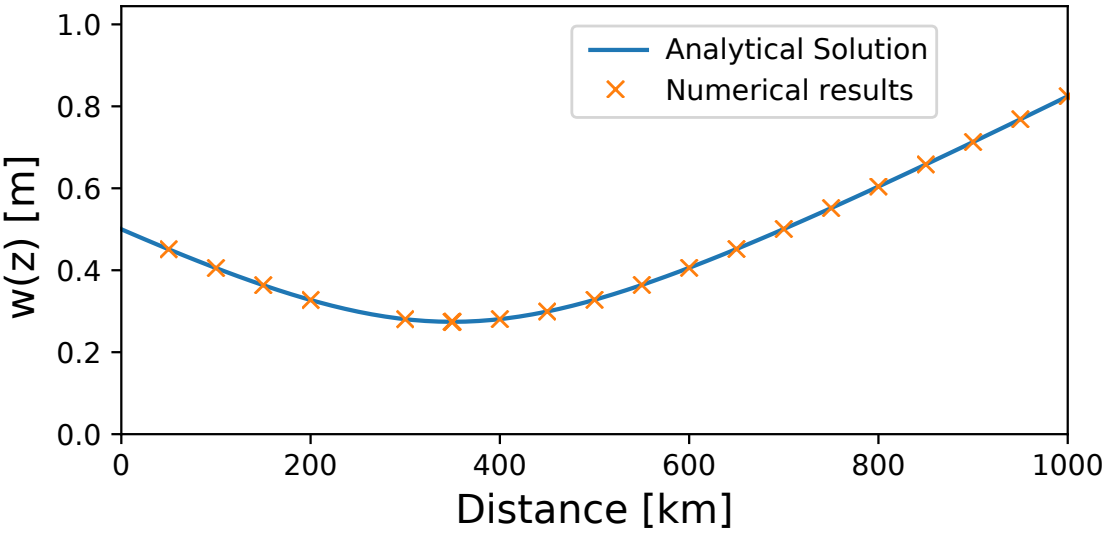

Figure 4.1: Beam radius along the propagation axis,showing the analytical solution and the numerical results.

Having calculated the beam properties analytically, AtmProp was used to propagate the undisturbed beam, without atmospheric influence. As the analytical formulae assume an unperturbed gaussian beam, no aperture has been assumed in the numerical simulation.
Figure 4.1 shows the radius of the beam as a function of the distance from the telescope. The wave-optical focus which equals the minimum beam radius is not at the zero position due to the shift of coordinates described beforehand. As can be seen for the nonturbulent case, the numerical results are identical to the analytical solution, showing that AtmProp captures the propagation behaviour in agreement with the analytical model. In addition to the beam-radius along the propagational axis the intensity profile in the radial direction has been analysed at z = 500 km and compared to the numerical result calculated by AtmProp and to the analytical solution (figure 4.2).
Calculation of the intensity for the analytical solution was done with equation (4.5) using the value for the beam radius at the desired position, the x coordinate representing radial coordinates.

$$I(x) = \frac{2P}{\pi w^2(z_{wave})} e^{\frac{-2x^2}{w(z_{wave})^2}} \tag{4.5}$$

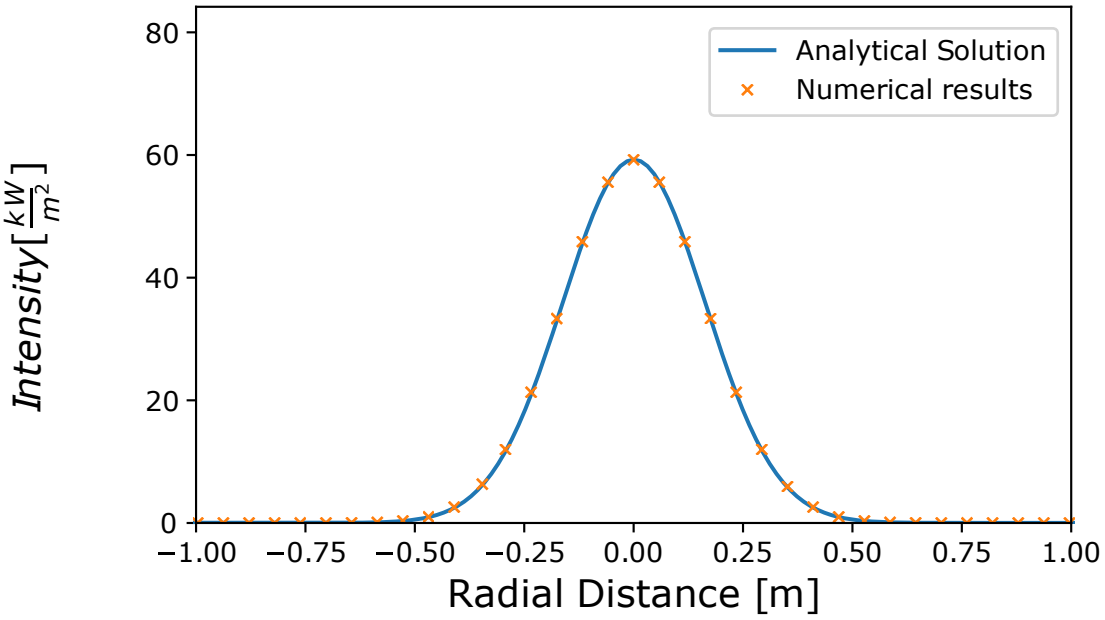

Figure 4.2: Radial profile of the intensity at z = 500 km for the reference beam without turbulence.

Both graphs are showing a good agreement between the analytical solution for a specified gaussian beam and the results from AtmProp. For future simulations one has to keep in mind that AtmProp's input parameter "InitialROC" has to be twice the radius of curvature of the wavefront because the input parameter of AtmProp refers to the the radius of curvature of the telescopes mirror and not the one of the wavefront.

4.2 Different turbulence models

To demonstrate the differences distinguishing the different models for atmospheric turbulence an example beam has been computed and propagated with all three models.The parameters used for the numerical calculation is shown below:

- Wavelenght: $\lambda = 1030\,nm$
- Grid size: 256 x 256 cells and 1600 x 1600 cm^2
- Number of averaging runs: 100
- Initial power: $10\,kW$
- Initial beam radius: $w_{init} = 178\,cm$
- Aperture usage: no
- Radius of curvature: $1000\,km$
- Final propagation distance: $600\,km$

The parameters used for the turbulence models used in this simulation are the same used to compute the examples of the according turbulence distributions in figure 2.7 for the HV

model, in figure 2.8 for the HAP model and in figure 2.9 for the ARL model.
The resulting turbulence distributions are shown in figure 4.3.

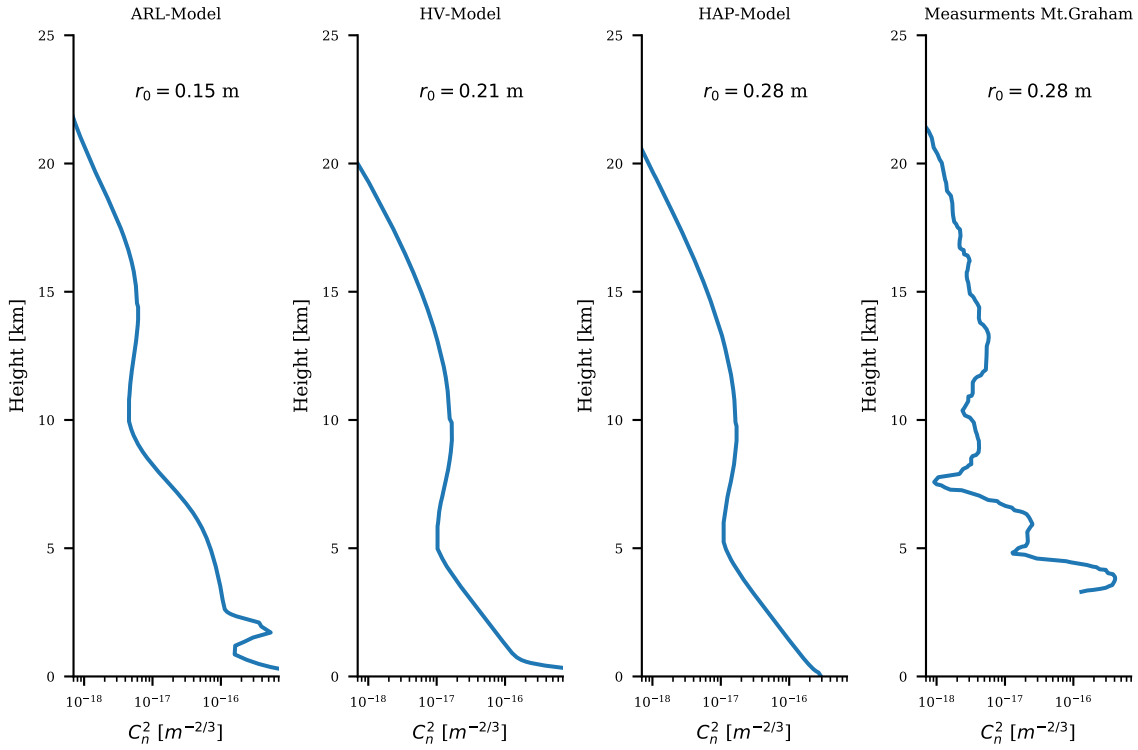

Figure 4.3: Turbulence models used for this comparison.

4.2.1 Results

Table 4.1 is showing the analytical and the numerical results. Shown is the turbulence model used, the numeric beam radius $w_{numeric}$, the coherence diameter r_0, the analytic beam radius $w_{analytic}$ and the quotient $\frac{w_{numeric}}{w_{analytic}}$.

Turbulence model	$w_{numeric}$ [m]	r_0 [m]	$w_{analytic}$ [m]	$\frac{w_{numeric}}{w_{analytic}}$
ARL	3.55	0.15	3.62	0.98
HV	3.29	0.21	2.69	1.22
HAP	2.01	0.277	2.04	0.98
Measurements	1.77	0.283	1.98	0.89

Table 4.1: Tabular overview of results for the four different calculations.

It turns out that although the HAP-model and the HV-model are similar regarding the $C_n^2(h)$ values the resulting laser beam is different, judging by table 4.1 and figure 4.4. The important difference here is the difference of the turbulence distribution close to the ground.
Masciadri et al. indicated in their Paper that in their measurement "We find that around

50% of the turbulence developed in the whole atmosphere is concentrated below 80 ± 15 m from the ground and 60% of the turbulence in the first kilometre".The results shown here are agreeing with this Paper regarding the fact that apparently the important part of the Atmosphere for the Propagation of a Laser beam to a satellite in an orbit is the lower part and not the higher parts of the earths Atmosphere.This coincidences with the fact that most bigger telescopes worldwide are located on mountains and other raising landmarks.
Figure 4.4 is showing the four different laser beam profiles resulting from the numerical calculation.

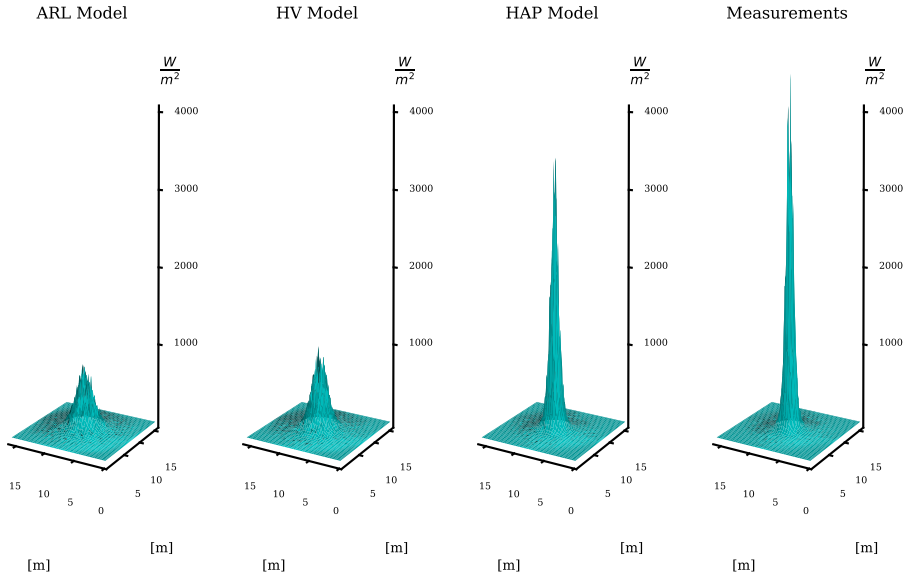

Figure 4.4: 3D beam profiles for this comparison.

4.3 Turbulence and constant ROC

The influence of turbulent effects according to the numerical model have been compared to the result of the analytical equations [11] [4] [9]. To model the turbulence a HAP model for $C_n^2(h)$ was used with a fixed value $p = \frac{4}{3}$ for modelling the turbulence ground layer distribution of the C_n^2 values.Therefore, exceeding this height, the propagation is continued without turbulence effects, by setting the structure constant to zero.
The other parameters of the turbulence model are the same than mentioned in figure 2.8. The turbulence distribution used for the comparison is shown in figure 4.5. The following list shows which parameters have been used for the calculation in this subsection.

- Grid size: 256 x 256 cells and 1600 x 1600 cm^2
- Number of averaging runs: 100
- Initial power: 10 kW
- Initial beam radius : 50 cm
- Aperture usage: no
- Initial radius of curvature of the telescope mirror: 1000 km (mirror)
- Final propagation distance: 1000 km
- $C_n^2(0)$: 1.7e-14 $m^{-2/3}$

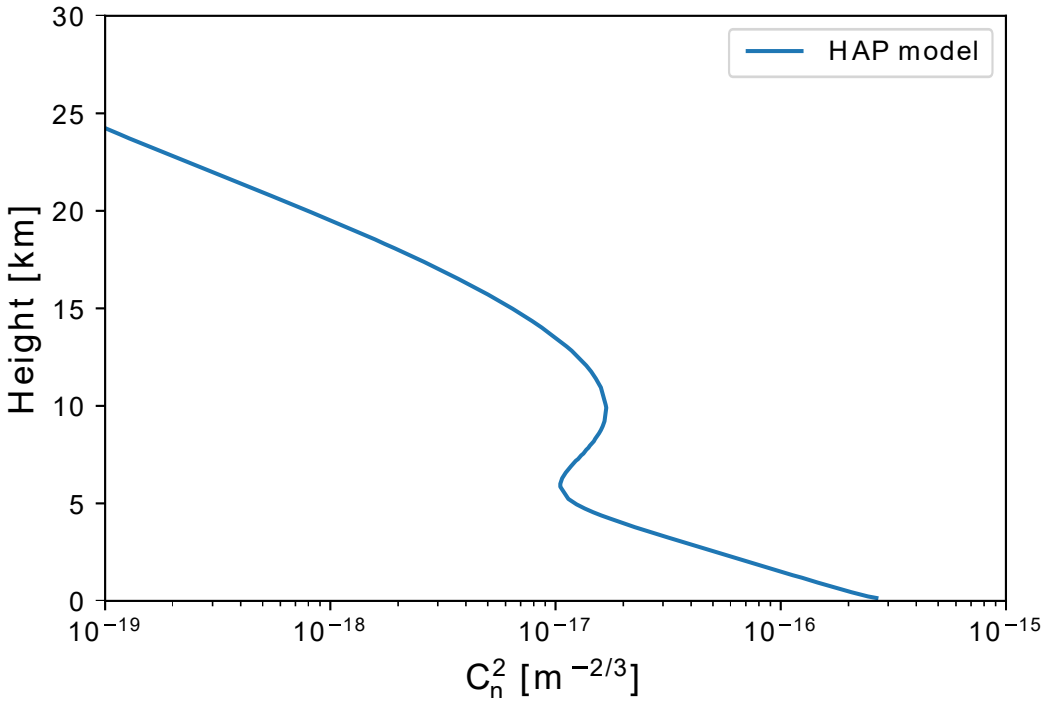

Figure 4.5: $C_n^2(h)$ for the case described in this subsection.

4.3.1 Results

Distance [km]	$w_{numeric}$ [m]	r_0 [m]	$w_{analytic}$ [m]	$\frac{w_{numeric}}{w_{analytic}}$
50	0.47	0.313	0.48	0.979
100	0.49	0.301	0.51	0.96
200	0.66	0.295	0.71	0.929
300	0.90	0.293	0.99	0.910
400	1.19	0.291	1.30	0.915
500	1.49	0.29	1.63	0.914
600	1.78	0.289	1.96	0.908
700	2.08	0.288	2.30	0.904
800	2.37	0.288	2.64	0.898
900	2.74	0.287	2.99	0.916
1000	3.01	0.287	3.33	0.904

Table 4.2: Tabular overview of values shown in figure 4.6, calculated with a constant initial radius of curvature.

Table 4.2 shows a comparison between analytic and numeric results for the beam radius as a function of distance from the zero coordinate which is located at the exit of the telescope similar to the non-turbulent propagation of the reference beam discussed beforehand. Note that each propagation run returns a laser profile which is not gaussian or regular any more and neither elliptic nor circular.
AtmProp is calculating the 2nd order moment of the resulting beam regardless of the beam shape, in both directions x and y which are perpendicular to the propagation direction. To calculate a beam comparable to the analytical solution a circular profile is calculated with the two 2nd order moments according to equation (4.6).Looking at the projection of the beam onto the x,y plane this circular profile exhibits the same area than the numerical results.
The beam radius r_{circ} is representing $w_{numeric}$ in the following sections.

$$r_{circ} = \sqrt{r_x \cdot r_y} \tag{4.6}$$

The coherence diameter r_0 was calculated according to equation (3.5). It is a result of the turbulence model and the propagated distance, the zenith angle ζ was set to zero here. The analytical beam radius is calculated from equations (3.4). Note that r_0 should be identical in the numeric and in the analytic analysis.
This was realized by calculating the coherence diameter from the $C_n^2(h)$ discretization used as an input for the numeric calculations.
The results are presented in Table 4.2 as well as in Figure 4.6. This figure shows two different lines. The beam radius is calculated numerically (green line) and analytically (orange line) using the same coherence radius for both calculations.
It can be seen that identical system and turbulence settings lead in both methods to similar results with the biggest deviation occurring at 1000 km from the telescope exit.

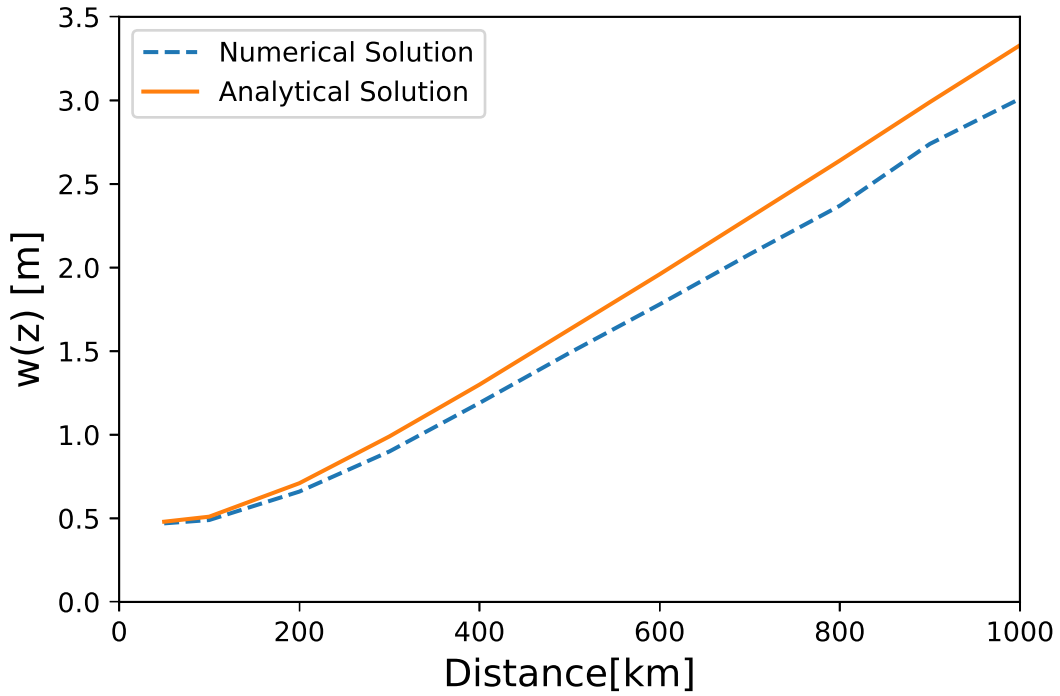

Figure 4.6: Beam radius along the propagation axis for the numerical solution and the analytical solution showing the values from table 4.2

.

The two laser beam profiles can be seen in figure 4.7a.
Of this lines the green one shows the resulting averaged beam profile, the blue one shows the analytical gaussian beam calculated with the according coherence diameter r_0.
The x-Axis is pointing in the radial direction perpendicular to the propagation vector and the actually three-dimensional intensity distribution is shown two-dimensional as a cross section.

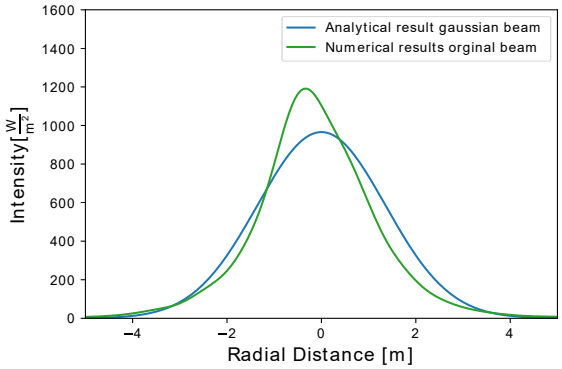

(a) Beam intensity profile in radial direction.

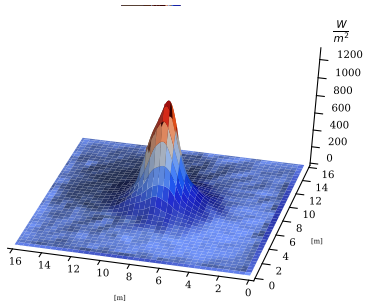

(b) 3D visualization of the laser beam

Figure 4.7: Radial profile and 3D plot of the laser beam

4.4 Variable ROC and turbulence

To get an idea about the importance of the initial radius of curvature the gaussian reference beam is used again and calculated with a radius of curvature adapted to the final propagation distance, meaning that the geometrical optical focus is located in the final plane of the propagation.
The turbulence distribution used here is the one shown in figure 4.5, and the used parameters for the propagation are listed below.Table 4.2 shows the results of this simulation.
Figure 4.8 is showing the results of the numeric and of the analytic case where the ROC has been set to the final propagation distance similar to the case before with an orange and a blue line.For comparison the value from the case beforehand with the constant ROC have been included marked by the green and red crosses.

- Grid size: 256 x 256 cells and 1800 x 1800 cm
- Number of runs: 100
- Initial power: 10 kW
- Initial beam radius : 50 cm
- Aperture usage: no
- Final propagation distance: 1000 km

Distance [km]	$w_{numeric}$ [m]	r_0 [m]	$w_{analytic}$ [m]	$\frac{w_{numeric}}{w_{analytic}}$	ROC [km]
100	0.280	0.301	0.315	0.889	200
200	0.590	0.295	0.642	0.919	400
300	0.853	0.293	0.971	0.878	600
400	1.162	0.291	1.301	0.893	800
500	1.4589	0.290	1.631	0.894	1000
600	1.733	0.289	1.962	0.883	1200
700	2.044	0.288	2.293	0.891	1400
800	2.330	0.288	2.626	0.887	1600
900	2.650	0.287	2.959	0.896	1800
1000	2.9748	0.287	3.292	0.903	2000

Table 4.3: Tabular overview of values shown in figure 4.6, calculated with the initial radius of curvature set to the propagation distance

4.4.1 Results

Comparing the two results it becomes clear that the difference is occuring at distances close to the telescope but moving further away from the "start" of the beam the difference starts to become negligible and, interestingly, the difference between the analytic solution and the numeric solution starts to grow approaching 1000 km propagation distance. It can be clearly seen in this case that the diameter of the beam is not influenced by the initial radius of curvature neither according to the analytic model nor to the numeric model.They agree pretty well in both cases with the exception of distances of 0-200 km from the telescope. Additionally, a influence of the radius of curvature can be seen in this area.Figure 4.9a shows a cross

section of the intensity profile of the propagated beam similar to figure 4.7, for an analytical beam calculated with the coherence diameter for the according turbulence distribution, the gaussian beam computed with the resulting 2nd moment and the actual beam profile which was computed by the numerical code.

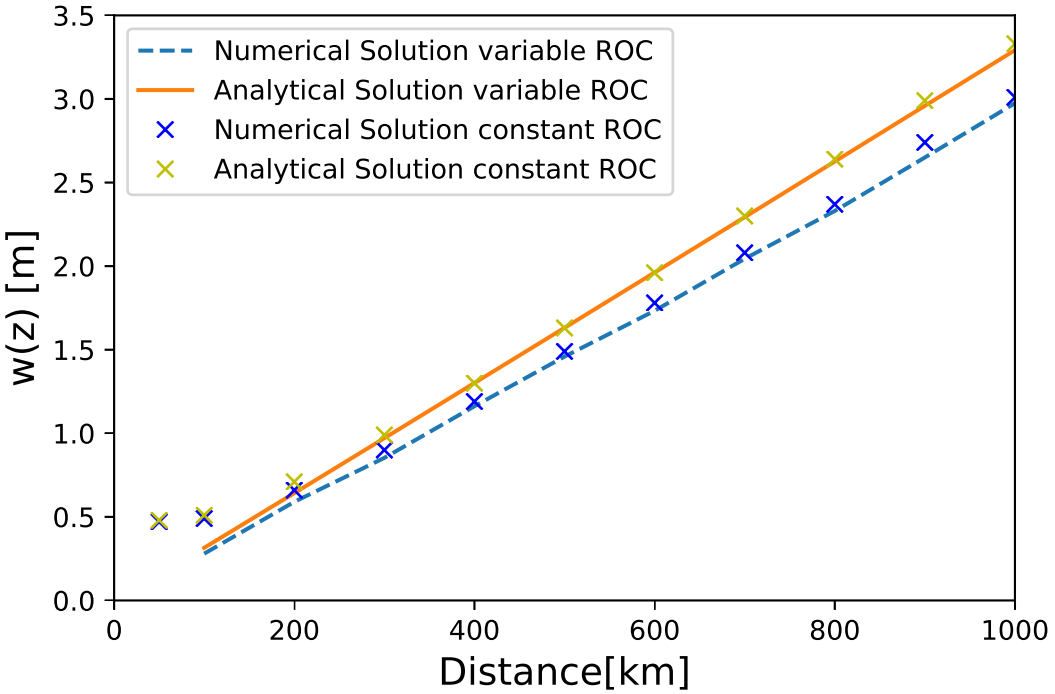

Figure 4.8: Beam radius along the propagation axis, averaged over 100 runs. Shown are both cases, one with the ROC set to a constant value and one with the ROC adapted to the final propagation distances.

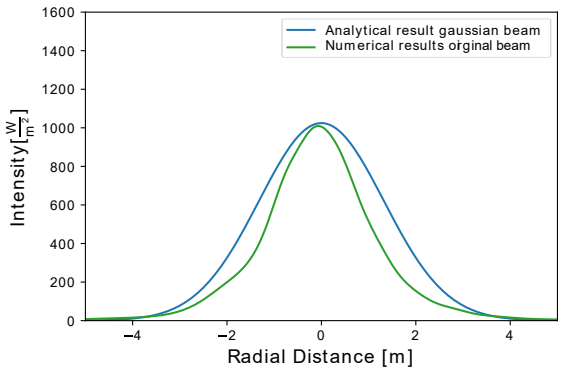

(a) Beam intensity profile in radial direction at z =1000 km, averaged over 100 runs.

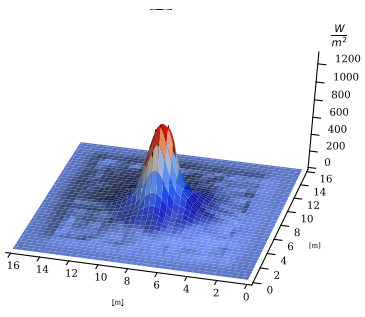

(b) 3D visualization of the laser beam

Figure 4.9: Radial profile and 3D plot of the laser beam

Looking at these results two conclusions can be drawn, the first one is that in addition to the non-turbulent reference beam the numerical model is also capable of modelling the turbulent

case with a given height distribution of the turbulent values.The second one is that the radius of curvature of the initial beam is not very important for the beams final diameter in the case of bigger distances.

4.5 Varying beam diameter

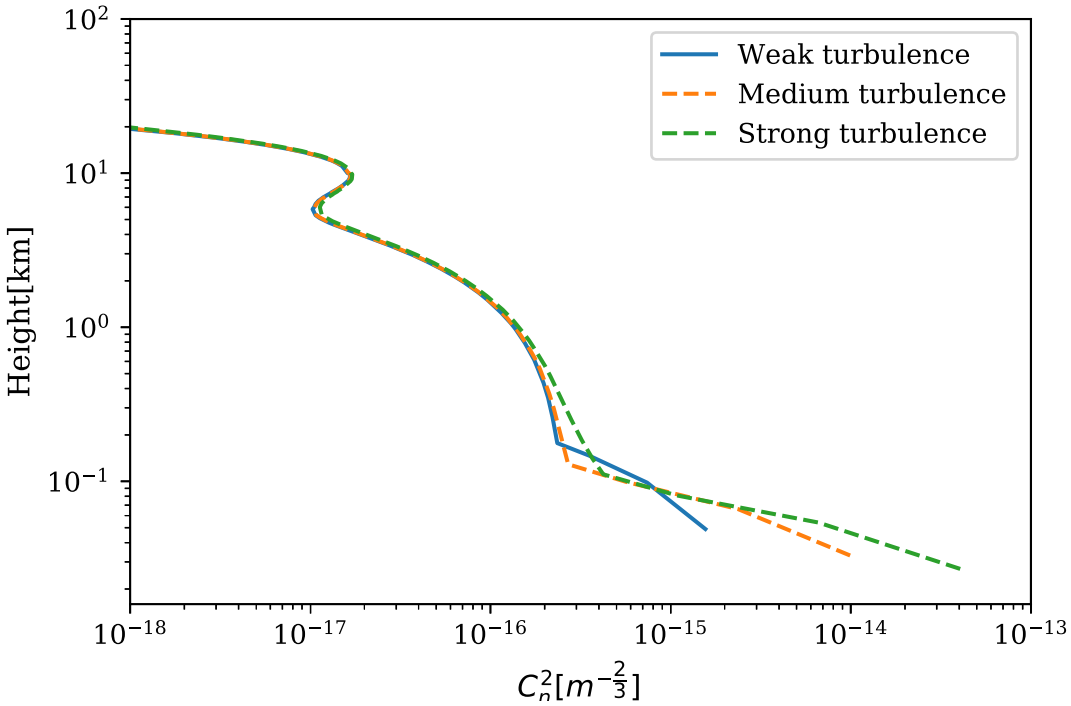

Figure 4.10: Used turbulence models for the varying beam diameter experiment, with $C_n^2(0) = 2 \cdot 10^{-15}$, $2 \cdot 10^{-14}$, $1 \cdot 10^{-13}$ $[m^{-\frac{2}{3}}]$.The higher the value the lower is the turbulence.All other paramters used for the HAP model are the same than in figure 2.8.

Next a series of simulations have been conducted, with the aim to gain insight about the influence of the beam diameter with a set of three different turbulence conditions.
Using the HAP turbulence model with three different input parameters for $C_n^2(0)$ which are $C_{n_{low}}^2(0) = 2 \cdot 10^{-15}\, m^{-\frac{2}{3}}$, $C_{n_{medium}}^2(0) = 2 \cdot 10^{-14}\, m^{-\frac{2}{3}}$ and $C_{n_{strong}}^2(0) = 1 \cdot 10^{-13}\, m^{-\frac{2}{3}}$ for the low turbulence case, the medium turbulence case and the strong turbulence case.
Tables 4.4, 4.5 and 4.6, are showing the results for this simulations.
The first column shows the inital beam diameter,the second one the beam diameter assumed as a gaussian beam as discussed beforehand.
Following this is the coherence diameter calculated with the equation (3.5) in the third column.
The fourth column is showing the beam diameter of the analytic equations computed with the coherence diameter and the other parameters being the same than in the numeric simulation.
Finally, the fifth column shows the quotient of the numeric beam radius and the analytic beam radius.

It has to be noted here that the results for the beam with the initial radius $w_{init} = 35.75\,cm$ might contain errors and are not accurate.
The other relevant parameters are shown in the list below and they are kept the same for all turbulence strength levels.

- Grid size: 512 x 512 cells and 2400 x 2400 cm^2
- Number of runs: 100
- Initial power: 10 kW
- Aperture usage: no
- Initial radius of curvature: 2000 km
- Wavelength: 1064 nm
- $C_n^2(0) = 2 \cdot 10^{-15}$, $2 \cdot 10^{-14}$, $1 \cdot 10^{-13}$ $[m^{-\frac{2}{3}}]$
- Final propagation distance : 1000 km

Figure 4.10, shows the three different turbulence distributions used for calculating the three different cases, the blue solid line is representing the weak turbulence case, the orange one the medium strength turbulence case. The green line is representing the case of strong turbulence. It becomes obvious that the distributions are not different a lot regarding their values in bigger heights, but they do differ in the proximity of the ground. This region is the most important one for the turbulent impact onto the propagation of the laser beam as pointed out before. In order to highlight this difference the graph has been drawn with two logarithmic axes.

4.5.1 Low turbulence

Comparing the results for the different initial beam radii, it can be seen that both the numeric and the analytic beam diameter have the tendency of converging to a fixed value for the beams diameter.
Hence similar to the radius of curvature being looked at beforehand it can be concluded from this simulations that the beams diameter in the target orbit can be only merely changed by changing the initial beam diameter.

Initial beam diameter [cm]	$w_{numeric}$ [m]	r_0 [m]	$w_{analytic}$ [m]	$\frac{w_{numeric}}{w_{analytic}}$
35.75	3.175	0.283	3.52	0.90
71.50	3.315	0.283	3.43	0.97
107.2	3.474	0.283	3.408	1.02
143.00	3.532	0.283	3.401	1.04
178.80	3.564	0.283	3.390	1.05
214.50	3.599	0.283	3.391	1.06

Table 4.4: Tabular overview of results for different beam diameters with a $C_n^2(0) = 2 \cdot 10^{-15}\, m^{-\frac{2}{3}}$.

Although the analytic and the numeric solutions are both converging to a constant value they are not approaching the same values.

Hence the quotient of $w_{numeric}$ and $w_{analytic}$ is also converging in the case of low turbulence it starts with a value of 0.90, for the smallest beam and converges to 1.06 for the largest beam. Figure 4.11 is showing the final beam radius in the target orbit as a result of the initial beam radius in the case of weak turbulence, the good agreement between the analytic and the numeric solution can be clearly seen here, the difference is maximum ten percent for all cases.

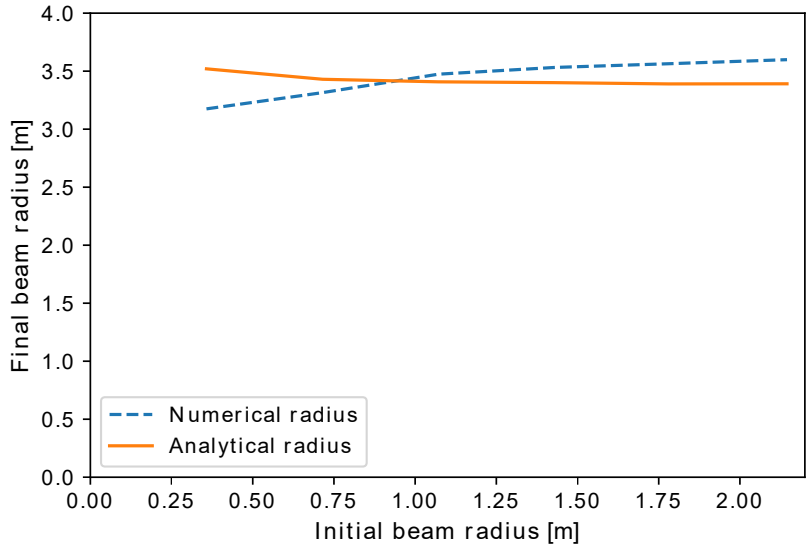

Figure 4.11: Final beam radius at final propagation distance over initial beam diameter at the sending telescope for low-turbulence conditions.

Figure 4.12 shows the intensity distribution at the target distance, 1000 km for all initial beam diameters considered in the case of the varying beam diameter simulations. The y- and x-axis are shown in $[m]$ while the z-axis is showing the intensity in $\frac{W}{m^2}$. Each subfigure is showing a different initial beam diameter ranging from $36cm$ in subfigure 4.12a to 215 cm in subfigure 4.12f.
Subfigure 4.12a is showing the typical pattern of a calculation where the fourier space is chosen to small: A slight square pattern is visible around the laser beam which is indicating that for this beam diameter the fourier space has to be set to a higher value.

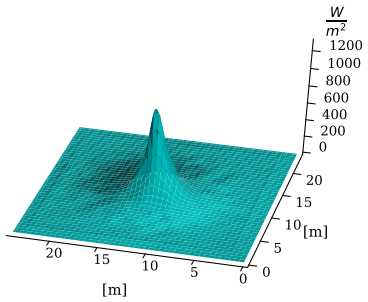

(a) Initial beam radius w_{init} = 36 cm

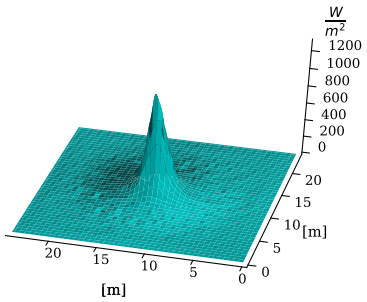

(b) Initial beam radius w_{init} = 72 cm

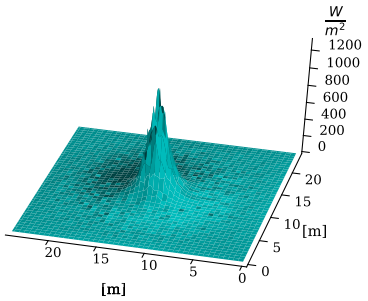

(c) Initial beam radius w_{init} = 107 cm

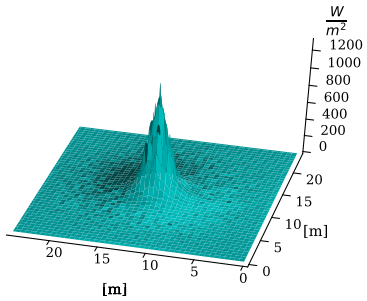

(d) Initial beam radius w_{init} = 143 cm

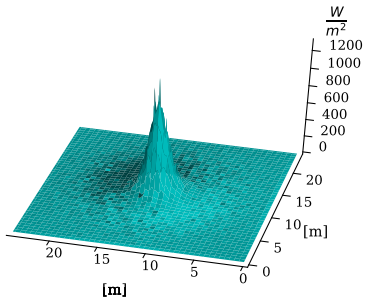

(e) Initial beam radius w_{init}= 178 cm

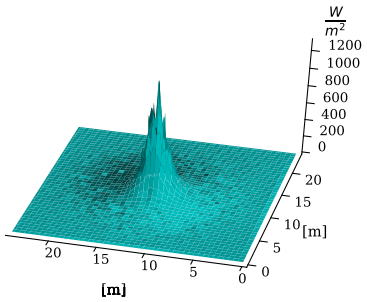

(f) Initial beam radius w_{init} = 215 cm

Figure 4.12: Beam shapes at final propagation distance for different values of initial beam radius w_{init}, and low-turbulence conditions.

4.5.2 Medium turbulence

The same simulation has been conducted with higher turbulence close to the ground, while all other parameters have been set to constant and only the beam diameter has been varied.
Again, the difference between the analytic and the numeric solution is in the focus of analysing the results of this simulations.
With increasing level of turbulence the coherence diameter is decreasing, and the beam's final diameter is increasing for the analytic and the numeric simulations.
The amount of increase is different for the analytic case and the numeric case. Compared to the case of low-turbulence the final beam diameter of the numeric solution rises by 28 % and the analytic case by 11 % regarding the value the solutions are converging onto.
As a consequence the quotient of both beam diameters is rising as well. In contrast to the low turbulence case the two models exhibit differences up to 16 %

Inital beam diameter [cm]	$w_{numeric}$ [m]	r_0 [m]	$w_{analytic}$ [m]	$\frac{w_{numeric}}{w_{analytic}}$
35.75	4.08	0.24	4.10	0.995
71.50	4.43	0.24	4.02	1.102
107.2	4.50	0.24	4.00	1.13
143.00	4.58	0.24	3.99	1.15
178.80	4.59	0.24	3.99	1.15
214.50	4.63	0.24	3.99	1.16

Table 4.5: Tabular overview of results for different beam diameters with a $C_n^2(0) = 2 \cdot 10^{-14} m^{-\frac{2}{3}}$.

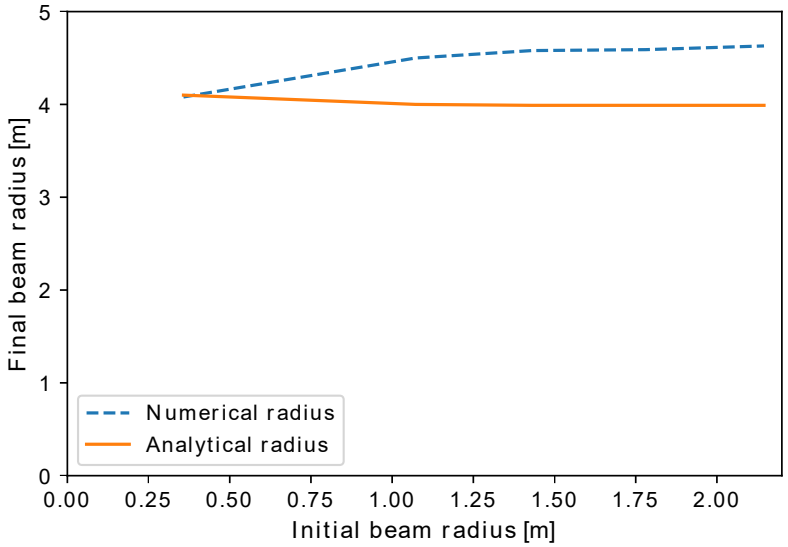

Figure 4.13: Final beam radius at final propagation distance over initial beam diameter at the sending telescope for medium-turbulence conditions.

Figure 4.13 is showing again the final beam radius as an result of the initial beam radius, similar to figure 4.11 with one difference which has to be noted here: For the numeric solution

of the weak turbulence the final beam diameter is below the analytic solution but is exceeding it for increasing initial beam diameters.In the case of medium turbulence the numeric solution is giving a bigger beam radius for nearly all initial beam diameters.
Figure 4.14 shows similar intensity distributions as figure 4.12. The difference is that here the profiles shown are for the case of medium atmospheric turbulence.
The square pattern for the smallest beam is visible here as well in subfigure 4.14a.

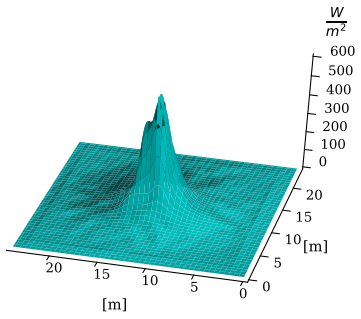

(a) Initial beam radius $w_{init} = 36$ cm

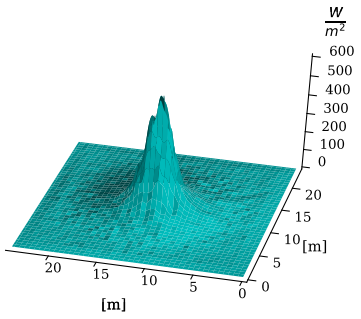

(b) Initial beam radius $w_{init} = 72$ cm

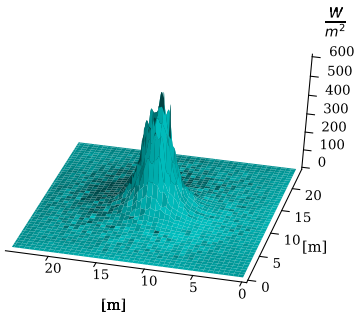

(c) Initial beam radius $w_{init} = 107$ cm

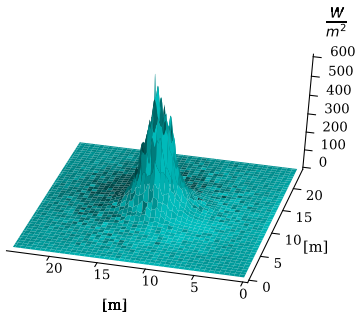

(d) Initial beam radius $w_{init} = 143$ cm

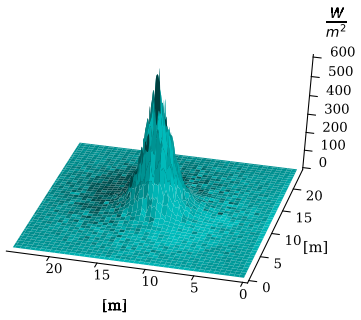

(e) Initial beam radius $w_{init} = 178$ cm

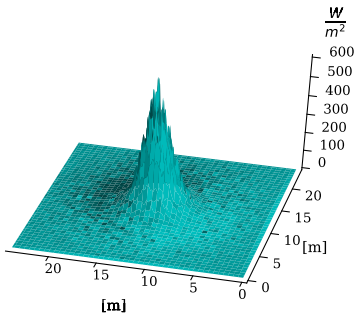

(f) Initial beam radius $w_{init} = 215$ cm

Figure 4.14: Beam shape at final propagation distance for different values of initial beam radius w_{init}, and medium-turbulence conditions.

4.5.3 Strong turbulence

In the case of strong turbulence the trend observed comparing the case of the medium turbulence and the weak turbulence is continuing. For the biggest beam diameter the final value of the beam diameter is increasing by 35 % for the analytic case while the numeric case is increasing by 26 % compared to the medium turbulence. Interestingly the increment of the beams diameter from the medium turbulence to the strong turbulence is exhibiting a lower difference between the numeric solution and the analytic solution. Hence the quotients in this case are also not increasing as strong as beforehand indicating that the difference of the analytic and the numeric method could converge to a constant value.

Inital beam [cm]	$w_{numeric}$ [m]	r_0 [m]	$w_{analytic}$ [m]	$\frac{w_{numeric}}{w_{analytic}}$
35.75	6.003	0.177	5.492	1.09
71.50	6.188	0.177	5.431	1.14
107.2	6.340	0.177	5.419	1.17
143.00	6.441	0.177	5.415	1.19
178.80	6.486	0.177	5.413	1.20
214.50	6.534	0.177	5.410	1.21

Table 4.6: Tabular overview of results for different beam diameters with a $C_n^2(0) = 1 \cdot 10^{-13} m^{-\frac{2}{3}}$.

Figure 4.15 is showing the final beam diameter as a function of the initial beam diameter for the case of strong turbulence. Obviously, the analytic model and the numeric model are not agreeing for calculating the beam diameter in the target orbit, although they depict a similar behaviour regarding the convergence tendency towards a constant beam diameter.

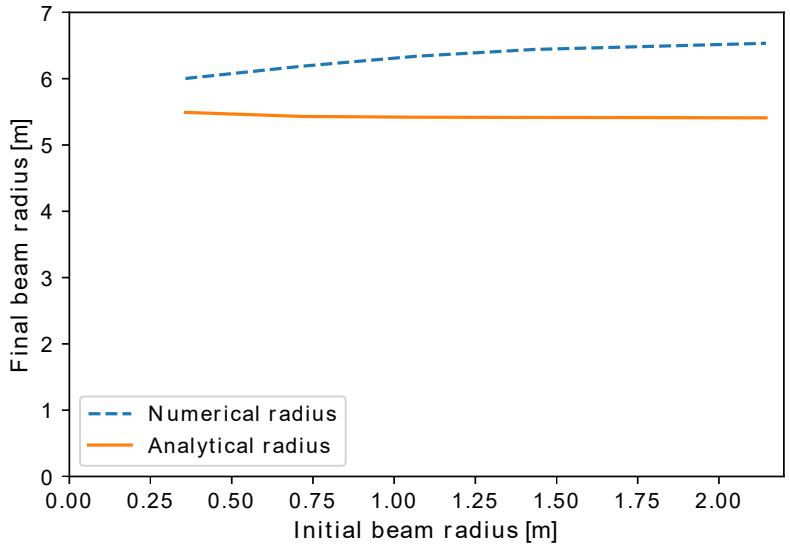

Figure 4.15: Final beam radius at final propagation distance over initial beam diameter at the sending telescope for strong-turbulence conditions.

Figure 4.16 shows the three dimensional intensity profile of the beam at the target distance of 1000 km for the case of strong turbulence, in the same way than figure 4.14 and figure 4.12.

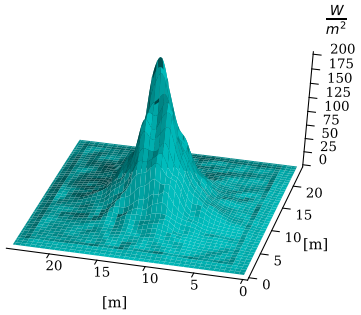

(a) Initial beam radius $w_{init} = 36$ cm

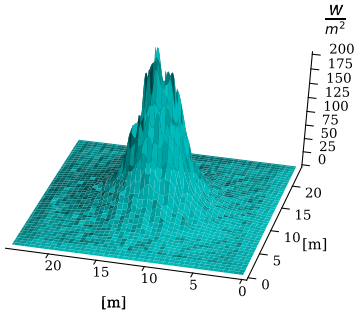

(b) Initial beam radius $w_{init} = 72$ cm

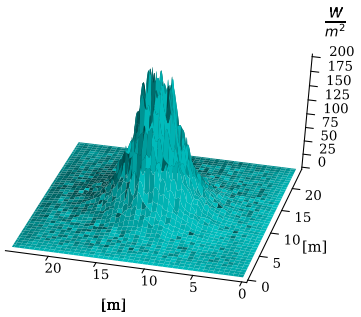

(c) Initial beam radius $w_{init} = 107$ cm

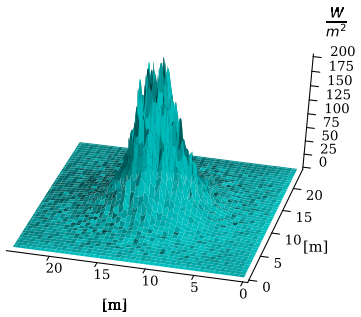

(d) Initial beam radius $w_{init} = 143$ cm

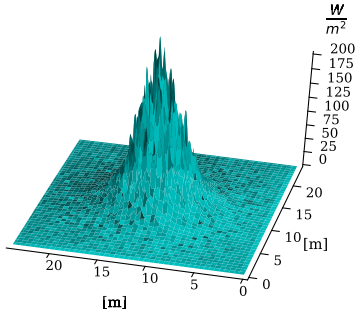

(e) Initial beam radius $w_{init} = 178$ cm

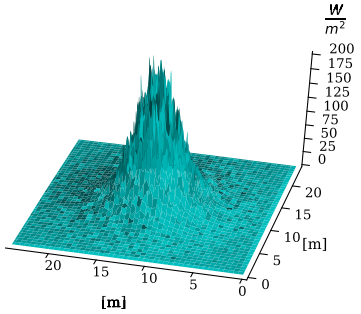

(f) Initial beam radius $w_{init} = 215$ cm

Figure 4.16: Beam shape at final propagation distance for different values of initial beam radius w_{init}, and strong-turbulence conditions.

4.5.4 Results

The results of the simulations with a varying beam diameter are showing that both solutions are converging to a constant value with increasing beam diameter. This constant value differs from 6 % in the low turbulence case to 16 % in the medium turbulence case and to 21 % in the high turbulence case, comparing the numerical and the analytical results. The numerical solution is predicting higher values in general.
For this simulations it can be seen that the results for the smallest beam with $w_{init} = 36\,cm$ have to be looked at sceptically due to the visible formation of a square pattern surrounding the beam profile in the plotted beam profiles.
This indicates that the chosen calculation radius is slightly too big, and therefore the fourier space becomes too small. Although the error is still small compared to the case of a fourier space which is way to small as shown in section 3.1.1. The maximum intensity for the beams doesn't vary much for the different beam diameters, as can be seen by comparing the visible maxima of the beams intensity distributions.
The most important result of this simulations is that the most important factor dictating the beam shape for the beam arriving at the target is the level of turbulence. The influence of the initial beam diameter is not having an significant effect on the final beam diameter. Therefore the simulations indicate that while designing a laser system for the use in a ground station, the designer is not strictly limited to a certain telescope diameter, considering the influence of atmospheric turbulence unless migitation of turbulence effects is considered.

4.6 Varying initial beam profiles

After studying the different beam diameters and the turbulent influence on them, the next step is to investigate different initial beam profiles. The beam profile which has been investigated till this point is exclusively the gaussian one. In addition to this a top-hat beam and a annular beam are propagated here.
The Top-Hat beam assumes a constant intensity across the whole aperture diameter, while the annular beam has a covered spot of 40 cm radius in the middle of the aperture. The gaussian beam used here has a w_{Init} of 143 cm.
The common parameters of this calculations are listed below:

- Grid size: 512 x 512 cells and 2400 x 2400 cm
- Number of runs: 100
- Initial power: 10 kW
- Aperture usage: 200 cm outer aperture radius
- Initial radius of curvature: 2000 km
- Wavelength: 1064 nm
- $C_n^2(0) = 2 \cdot 10^{-15}$, $2 \cdot 10^{-14}$, $1 \cdot 10^{-13}$ $[m^{-\frac{2}{3}}]$ (low,medium,high)
- Total propgation distance: 1000 km

The turbulence is modelled with the same three HAP models shown in figure 4.10, called "low","medium" and "high" turbulent levels. Therefore the coherence diameters are also the same for all three cases.

Table 4.7 shows the resulting beam radii for each case as well as the maximum Intensity after this 100 runs. The first column shows the turbulence model choosen, the second one the inital beam profile. This columns are followed by the numerical beam radius, the coherence diameter and the maximum intensity.

Turbulence level	Beam profile	$w_{numeric}$ [m]	r_0	Maximum Intensity $\left[\frac{W}{m^2}\right]$
low	Gauss	3.56	0.283	1151.36
medium	Gauss	4.60	0.24	628.59
high	Gauss	6.479	0.177	261.88
low	Top-Hat	3.889	0.283	1016.87
medium	Top-Hat	4.82	0.24	599.17
high	Top-Hat	6.648	0.177	295.84
low	Annular beam	3.93	0.283	975.61
medium	Annular beam	4.87	0.24	662.58
high	Annular beam	6.68	0.177	255.30

Table 4.7: Tabular overview of values for different beam profiles and different turbulence distributions and a propagation distance of 1000 km averaged over 100 runs for 1064 nm

Figure 4.17 is showing the cases of strong turbulence on the right side and the cases of low turbulence on the left side.The first line shows the gaussian profiles at the final propagation distance, followed by the Top-Hat profile and the annular profile in the lowest line.
As it can be seen the final shape of the beam does not vary for the three different inital profiles. Already with low turbulence the information about the beams shape is lost which can be clearly seen by the fact that the "blind spot" in the middle of the annular beam profile is not visible anymore. For strong turbulence it is exactly the same, the three beams are not distinguishable.

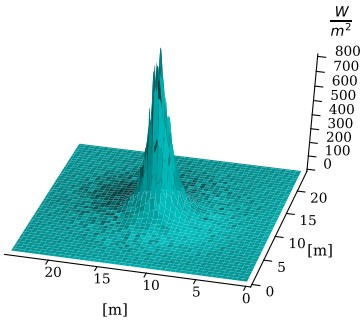

(a) Gaussian beam low turbulence

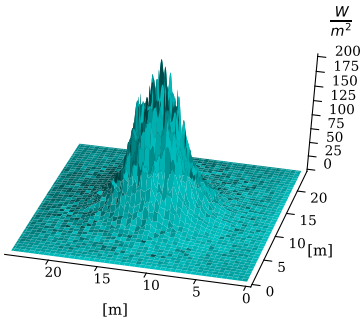

(b) Gaussian Profile strong turbulence

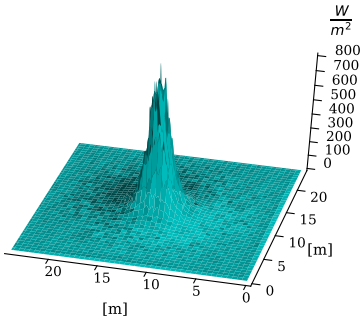

(c) Top-Hat Profile low turbulence

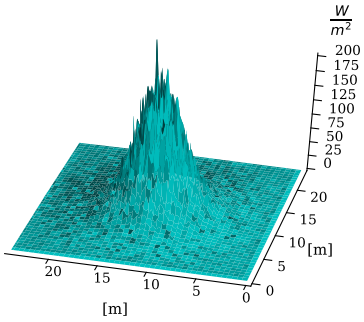

(d) Top-Hat Profile strong turbulence

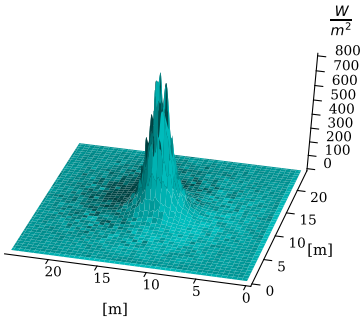

(e) Annular Beam Profile low turbulence

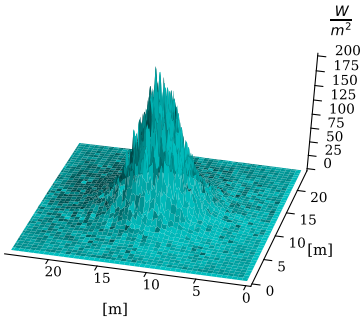

(f) Annular Beam Profile strong turbulence

Figure 4.17: Beam profiles at the final propagation distance for all three initial beam profiles, only low and strong turbulence levels are shown.

As a comparison the beams without any turbulent influence also have been propagated over the complete propagation distance. Figure 4.18 is showing the undisturbed gaussian profile on the upper left, the annular beam in the upper right the Top-Hat on the bottom, after a propagation of 1000 km with an aperture radius of 200 cm in the beginning. Note the altered scale compared to figure 4.17. In contrast to the turbulent case there is a difference visible, comparing the different types of beams. The ring patterns surrounding the beams differ for each beam, and in addition the maximum intensity of the beams is different.

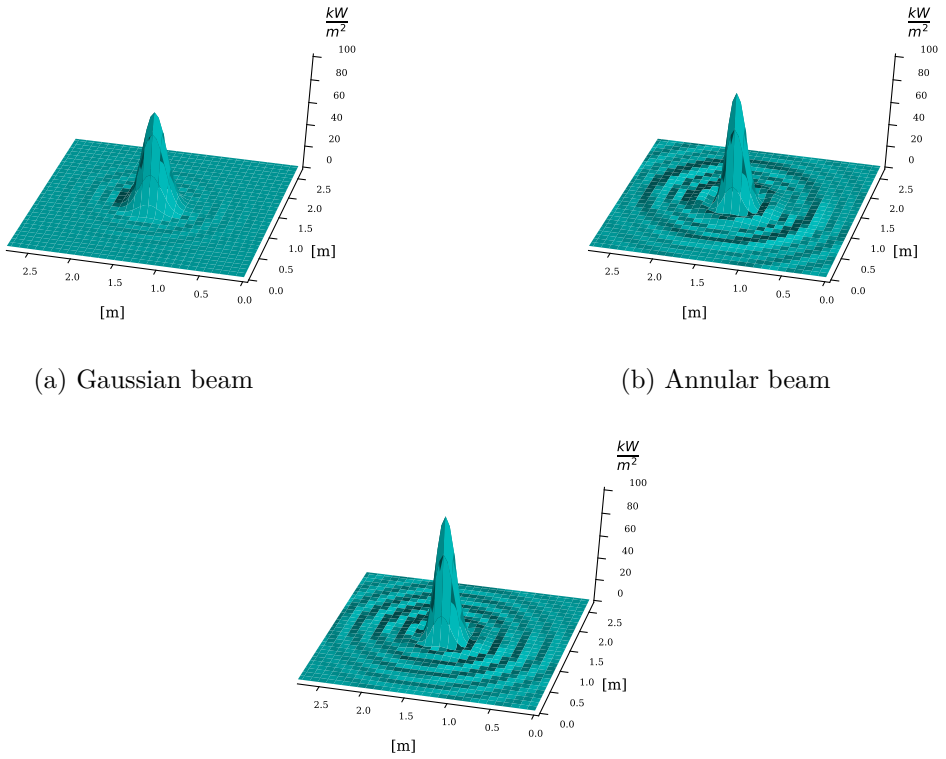

(a) Gaussian beam

(b) Annular beam

(c) Top-hat beam

Figure 4.18: Single shots for all three beam profiles with aperture, without turbulence influence.

Note, that the ring structures in the Gaussian case stem from diffraction at the aperture edge. Note also, that the maximum intensities of the Top-Hat and Annular beams are larger than for the Gaussian beam. This feature is lost as soon as turbulence influences the propagation.

5 De-orbit of a satellite

This chapter is using data from the master thesis of Kevin Bergmann [5], which has its focus on the effect of laser radiation on a satellite, especially for post mission disposal operations. The idea is that a satellite has to be de-orbited after its mission is either accomplished or it is damaged in a way which is hindering it in fulfilling the mission it has been designed for.
This de-orbit is conducted by lowering the orbit of the satellite into a height where the atmospheric drag is having an effect.
In contrast to the work of Bergmann this thesis is focused on the modelling of the wave-optical propagation in the atmosphere and not on the effect on a satellite in the context of Post-mission disposal.
Hence only one simulation has been conducted to demonstrate that the concept of using an ablative propulsion unit and a ground based laser could potentially be used to achieve the goal of post mission disposal, taking down to account the atmospheric turbulence.
The laser system is assumed to have no turbulence compensation yet, which would improve the results.

5.1 De-orbit simulation

Since the numerical and the analytical model deviate only slightly the decision was taken to use the analytical model since the implementation into a orbit propagation tool is easier and faster to calculate.
The same formulae presented in section 3.2 where used to calculate the gaussian beam diameter at the target distance with the coherence diameter r_0 calculated as a function of the zenith angle ζ with equation (3.5).
The assumptions here are that the satellite with a mass of $m_{sat} = 150kg$, is starting at a circular orbit exhibiting an apogee height of $h_{apo} = 1000km$ and an inclination of $In = 98°$. From there it descents till arriving at a perigee height of $h_{peri} = 250km$ where the friction forces of the atmosphere take over the rest of the de-orbit, till the satellite breaks up and burns up. The apogee height and therefore the propagation distance stays constant during this manoeuvre.
The Δv is given to the satellite by a ablative propulsion unit with a unit receiving the laser beam and focussing it on a spot diameter of $D_{spot} = 1.76cm$. The laser receiver is assumed to have a circular shape with a diameter of $D_{rec} = 3m$. The laser system on the ground has an initial beam radius of $w_{init} = 1.43m$ with a telescope diameter of 4 m and geometrical focus at $f = 1000km$, $M^2_{laser} = 1.0$, and $\sigma_{jitter} = 0.02\,arcsec$.
Additionally the laser is assumed to be pulsed with a pulse energy of $E_P^{GS} = 412J$ and a repetition rate of $f_{Rep} = 1000Hz$. The atmospheric assumptions used for this calculation are:

- Atmospheric model: HAP, $C_n^2(0) = 2 \cdot 10^{-14}[m^{-\frac{2}{3}}]$
- Weather: Only one-third of LIC (Laser irridiation contact) used
- Atmospheric extinction for clear weather conditions

The tool used to calculate the descent is called GEMAT, further details regarding this tool and details regarding the satellite system, the orbit of the satellite and the orbital dynamics can be found in [5]. Figure 5.1 is showing the perigee height over the time in days for the conditions described above.

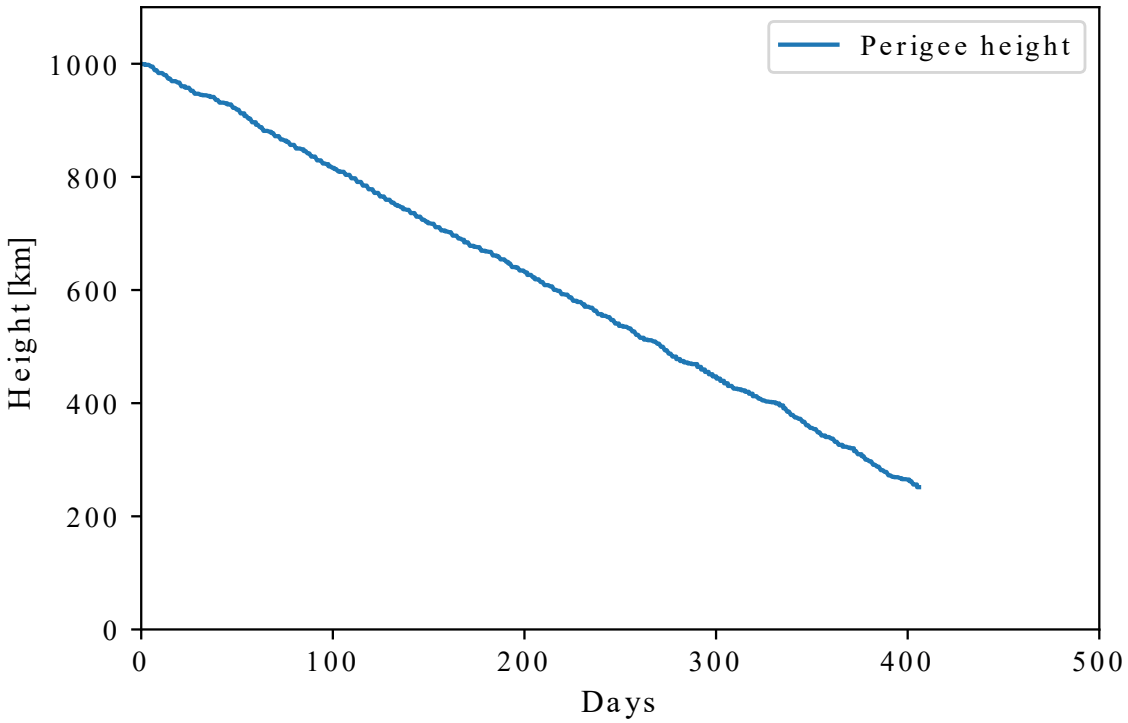

Figure 5.1: Development of the perigee height over time for the exemplaric de-orbit

The calculation is stopped as soon as the satellite is arriving at a pergigee height of 250 km which takes place after 1.11 years in the considered scenario.
Irridiation of the satellite takes place when the satellite orbit has a zenith angles from $\zeta = 60°$ to $\zeta = -60°$ with the zero angle defined as a vector perpendicular to the tangential plane along earths surface at the ground station.
Resulting from this is a a number of 0.474 passes per day with a averaged pass duration of 317 s.

5.2 Results

This case was calculated without any kind of turbulence compensation and is resulting in a acceptable time till the de-orbit is done. One issue here is that the laser needs to have a high repetition rate which is not realistic considering current systems [5]. Hence, a turbulence compensation will be necessary in order to use laser system which are available right now.

6 Summary and outlook

In the course of this thesis the wave-optical propagation of laser beam has been investigated with the tools AtmProp and the tool PropRunner, the second one has been developed with python during the course of this thesis.
Three different turbulence models for the turbulence distribution over height have been implemented, the first one being the famous HV model the second one the HAP model and the third one the ARL model. This enables the user of AtmProp to propagate through the earths atmosphere with taking atmospheric influence into account.
After this implementation the HAP model was mainly used for the calculations in this thesis which start with a verification of AtmProps functionality for a non-turbulent propagation which can be modelled analytically quite easily.
Next the beam diameter along a propagation is investigated with turbulent influence for a beam with a constant radius of curvature. In addition, the same calculation is conducted with the same coherence diameter and the analytical methods available for modelling the effect of turbulence on a laser beam propagating through the atmosphere.
The same calculation is repeated with the radius of curvature adapted to the relevant propagation distance, which is again compared to the analytical solution.
The result of this calculations is that the radius of curvature is not relevant for the beam diameter for bigger propagation distances. Furthermore they are showing that the numerical and the analytical method are giving similar results for the propagation.
For a set of beam diameters the resulting beam diameter at the target distance was calculated for three different realizations of the HAP model by varying the turbulence value on the ground.
Again the results where calculated with the analytical models as well as with the numerical models and have been compared, showing a difference but this difference is not very high. It is getting higher for increasing levels of turbulence though.
The most important result is that regarding the final beam diameter the chosen initial beam diameter is not important for big propagation distances, it is converging to a constant value in the end which is not influenced by the initial beam diameter.
The higher the turbulence is the less important is the initial beam diameter.
As a last simulation one beam diameter has been chosen to be compared with different initial beam profiles, moving away from the gaussian beam shape used to till this point.The two additional beam profiles have been a top-hat profile and a annular beam.
In this case a aperture was used limiting the inital beam and all three beam profiles have been propagated with the same three turbulence levels used for the different beam diameters beforehand.
The results are basically not varying a lot, comparing the three beam profiles although a slight difference can be seen in the final beam diameter.
The important fact which has to be noted here is that in contrast to the analytical model the intensity distribution at the target is known using the numerical results, which enables the user to use the beam profiles as input for designing optical systems on the target to make use of the incoming laser light for instance with an ablative propulsion unit delivering the Δv required for a post mission disposal.

The amount of information which can be calculated with the numerical model is higher compared to the analytical model which makes it more useful to estimate the usability of laser beams for space applications.In addition it was shown in this thesis that the results of this numerical simulations and the analytical solutions are not deviating too much.One has to be careful though because both are models with a set of assumptions which might produce errors comparing them with real-world experiments, and either one might prove to be closer to the measurements which have to be conducted at some point.
The agreement of both models is indicating though that measured results can be expected to be close to the real-world effects which has to be proven in future works.
One exemplaric de-orbit calculation shows that the concept can be considered feasible although a influence of the turbulence is effecting the laser beam.

7 Bibliography

[1] Andrews, L.C.: *Laser Beam Scintillation with Applications*, SPIE - The International Society for Optical Engineering, 2001

[2] Andrews, L.C.; Phillips, R.L.; Wayne, D.; Leclerc, T.; Sauer, P.; Crabbs, R.; Kiriazes, J.: Near-ground vertical profile of refractive-index fluctuations, in: *Atmospheric Propagation VI*, ed. Thomas, L.M.W.; Gilbreath, G.C., SPIE, may 2009

[3] Andrews, L.C.; Phillips, R.L.; Wayne, D.; Sauer, P.; Leclerc, T.; Crabbs, R.: Creating a profile as a function of altitude using scintillation measurements along a slant path, in: *High Energy/Average Power Lasers and Intense Beam Applications VI*, ed. Davis, S.J.; Heaven, M.C.; Schriempf, J.T.; Korotkova, O., SPIE, feb 2012

[4] Belmonte, A.: Feasibility study for the simulation of beam propagation: consideration of coherent lidar performance, *Applied Optics*, 39(30):5426, oct 2000

[5] Bergmann, K.: *Satellitenmodul für Post-Mission Disposal durch hochenergetische Laserstrahlung*, Master's thesis, RWTH Aachen, 2019

[6] Canuet, L.: *Atmospheric turbulence profile modeling for satellite-ground laser communication*, mathesis, Universitat Politècnica de Catalunya, July 2014

[7] Claus-Dieter Munz, T.W.: *Numerische Behandlung gewöhnlicher und partieller Differenzialgleichungen*, Springer-Verlag GmbH, ISBN 3662558858, 2019

[8] David H. Tofsted, S.G.O.: An Atmospheric Turbulence Profile Model for Use in Army Wargaming Applications 1, *Army Research Laboratory report*, 2006

[9] Dios, F.; Rubio, J.A.; Rodríguez, A.; Comerón, A.: Scintillation and beam-wander analysis in an optical ground station-satellite uplink, *Applied Optics*, 43(19):3866, jul 2004

[10] ESA,: *ESAs Annual Space Environment Report*, Tech. Rep., European Space Agency, 2019

[11] Fante, R.L.: Electromagnetic beam Propagation in Turbulent Media, *Proceedings of the IEEE*, 63(12), 1975

[12] Hodgson, N.: *Optical Resonators Fundamentals, Advanced Concepts and Applications*, Springer Verlag London, 1997

[13] J.A.Fleck,: Time-Dependent Propagation of High Energy Laser Beams through the Atmosphere, *Appl.Phys.10, 129 160(1976)*, 1976

[14] Kessler, D.J.: Collision Frequency of Artificial Satellites: The creation of a Debris Belt, *Journal of Geophysical research*, 83(A6):2637-2646, June 1978

[15] Kolmogorov, A.N.: *A refinement of previous hypotheses concerning the local structure of turbulence in a viscous incompressible fluid at high Reynolds number*, J.Fluid Mech, 1962

[16] Lamana, G.: *Selected Problem of Convective Heat Transfer*, Lecture slides, 2015

[17] Masciadri, E.; Stoesz, J.; Hagelin, S.; Lascaux, F.: Mt. Graham: optical turbulence vertical distribution with standard and high resolution, in: *Ground-based and Airborne Telescopes III*, ed. Stepp, L.M.; Gilmozzi, R.; Hall, H.J., SPIE, jul 2010

[18] Masciadri, E.; Stoesz, J.; Hagelin, S.; Lascaux, F.: Optical turbulence vertical distribution with standard and high resolution at Mt Graham, *Monthly Notices of the Royal Astronomical Society*, mar 2010

[19] NASA,: *Image from NASA*, Published on NASAs earthobservatory homepage, https://earthobservatory.nasa.gov/images/44267/sunset-from-the-international-space-station, Nov. 2019

[20] R.E.Hufnagel,: *The Infrared Handbook chapter 6, Propagation through atmospheric turbulence*, Office of Naval research, 1978

[21] Richardson, L.: *Weather prediction by numerical Process*, Cambridge Univ. Press, 1922

[22] Smith, F.G.: *The Infrared & Electro-Optical Systems Handbook*, Infrared Information Analysis Center, 1993

[23] Sparrow, E.M.; Husar, R.B.; Goldstein, R.J.: Observations and other characteristics of thermals, *Journal of Fluid Mechanics*, 41(4):793–800, may 1970

[24] Tatarski, V.: *Wave propagation in a turbulent medium*, McGraw-Hill, 1961

[25] Ulrich, P.: Hufnagel-Valley profiles for specified values of the coherence lenght and isoplanatic angle, *W.J. Schafer Associates*, 1988

[26] Valley, G.: Isoplanatic degradation of tilt correction and short-term imaging systems, *Appl. Opt. 19,574-577*, 1980

Acknowledgement

I would like to thank all people who have been involved in enabling me to write this thesis and conclude my studies of aerospace engineering at the University of Stuttgart with it. First my supervisor Jürgen Kästel for applying the right combination of pressure and freedom to me in the course of this thesis. Beside this he was always available for questions, finding weird errors in programs and helping me understand the complex physics and models i had to face during thit thesis. Furthermore i would like to thank Kevin Bergmann who worked in parallel on a related topic and always provided valuable insights in fruitful discussions. Stefan Scharring contributed indirectly through supervising Kevin, but the direct input i got from him always helped me a lot understanding the mystery of some topics regarding space. And of course i want to express my gratitude to Jochen Speiser for managing the department i had the possibility of writing my thesis in and Thomas Dekorsy for managing the whole institute and supervising my thesis. Also all my colleagues from the best student office in the fifth floor of building h who helped , added a lot to this thesis. Namely I had the pleasure to work in one office with Cristina, Annika, Julian and Francesco. Special thanks to Cristina who helped me a lot understanding the Institute and helping me not too forget the rest of my Spanish knowledge. Thanks to Julian for our coffee and smoking breaks, and giving valuable advices regarding live and my beard.

Statement of Originality

This thesis has been performed independently with support by my supervisors. It contains no material that has been accepted for the award of a degree in this or any other university. To the best of the candidate's knowledge and belief, this thesis contains no material previously published or written by another person except where due reference is made in the text. The electronic version is identical to the printed versions.

Date Signature